A&A 478, 371–385 (2008)
DOI: 10.1051/0004-6361:20078344
© ESO 2008

Astronomy & Astrophysics

Heating of blue compact dwarf galaxies: gas distribution and photoionization by stars in I Zw 18⋆

D. Péquignot

LUTH, Observatoire de Paris, CNRS, Université Paris Diderot; 5 place Jules Janssen, 92190 Meudon, France
e-mail: Daniel.Pequignot@obspm.fr

Received 24 July 2007 / Accepted 31 October 2007

ABSTRACT

Aims. Photoionization models so far are unable to account for the high electron temperature T_e([O III]) implied by the line intensity ratio [O III]λ4363 Å/[O III]λ5007 Å in low-metallicity blue compact dwarf galaxies, casting doubt on the assumption of photoionization by hot stars as the dominant source of heating of the gas in these objects of large cosmological significance.
Methods. Combinations of runs of the 1D photoionization code NEBU are used to explore alternative models for the prototype giant H II region shell I Zw 18 NW, with no reference to the filling factor concept and with due consideration for geometrical and stellar evolution constraints.
Results. Acceptable models for I Zw 18 NW are obtained, which represent schematically an incomplete shell comprising radiation-bounded condensations embedded in a low-density matter-bounded diffuse medium. The thermal pressure contrast between gas components is about a factor 7. The diffuse phase can be in pressure balance with the hot superbubble fed by mechanical energy from the inner massive star cluster. The failure of previous models is ascribed to (1) the adoption of an inadequate small-scale gas density distribution, which proves critical when the collisional excitation of hydrogen contributes significantly to the cooling of the gas, and possibly (2) a too restrictive implementation of Wolf-Rayet stars in synthetic stellar cluster spectral energy distributions. A neutral gas component heated by soft X-rays, whose power is less than 1% of the star cluster luminosity and consistent with CHANDRA data, can explain the low-ionization fine-structure lines detected by SPITZER. [O/Fe] is slightly smaller in I Zw 18 NW than in Galactic Halo stars of similar metallicity and [C/O] is correlatively large.
Conclusions. Extra heating by, e.g., dissipation of mechanical energy is not required to explain T_e([O III]) in I Zw 18. Important astrophysical developments depend on the 5% uncertainty attached to [O III] collision strengths.

Key words. galaxies: individual: I Zw 18 – galaxies: starburst – ISM: H II regions – stars: early-type – stars: Wolf-Rayet – atomic data

1. Introduction

The optical properties of Blue Compact Dwarf (BCD) galaxies are similar to those of Giant Extragalactic H II Regions (GEHIIR). Their blue continuum arises from one or several young Massive Star Clusters (MSC), which harbour extremely large numbers of massive stars.

BCDs are relatively isolated, small-sized, metal-poor galaxies (Kunth & Östlin 2000) and may be the rare "living fossils" of a formerly common population. BCDs can provide invaluable information about the primordial abundance of helium (e.g., Davidson & Kinman 1985), the chemical composition of the InterStellar Medium (ISM, e.g., Izotov et al. 2006a), the formation and evolution of massive stars, and the early evolution of galaxies at large redshift. Among them, I Zw 18 stands out as one of the most oxygen-poor BCDs known (e.g., Izotov et al. 1999) and a young galaxy candidate in the Local Universe (e.g., Izotov & Thuan 2004).

The line emission of H II regions is believed to be governed by radiation from massive stars, but spectroscopic diagnostics most often indicate spatial fluctuations of the electron temperature T_e (see the dimensionless parameter t^2, Peimbert 1967) that appear larger than those computed in usual photoionization models, suggesting an extra heating of the emitting gas (e.g., Peimbert 1995; Luridiana et al. 1999). Until the cause(s) of this failure of photoionization models can be identified, a basic tool of astrophysics remains uncertain.

Tsamis & Péquignot (2005) showed that, in the GEHIIR 30 Dor of the LMC, the various T_e diagnostics could be made compatible with one another if the ionized gas were chemically inhomogeneous over small spatial scales. A pure photoionization model could then account for the spectrum of a bright filament of this nebula. Although this new model needs confirmation, it is in agreement with the scenario by Tenorio-Tagle (1996) of a recycling of supernova ejecta through a rain of metal-rich droplets cooling and condensing in the Galaxy halo, then falling back on to the Galactic disc and incorporating into the ISM without significant mixing until a new H II region eventually forms. If this class of photoionization model is finally accepted, extra heating will not be required for objects like 30 Dor, with near Galactic metallicity.

Another problem is encountered in low-metallicity ("low-Z") BCDs (Appendix A). In BCDs, available spectroscopic data do not provide signatures for t^2, but a major concern of photoionization models is explaining the high temperature T_e([O III]) infered from the observed intensity ratio r([O III]) = [O III]λ 4363/([O III]λ 5007+4959). Thus, Stasińska & Schaerer (1999, SS99) conclude that photoionization by stars fails to explain r([O III]) in the GEHIIR I Zw 18 NW and that photoionization must be supplemented by other heating mechanisms.

⋆ Appendices are only available in electronic form at http://www.aanda.org

Article published by EDP Sciences and available at http://www.aanda.org or http://dx.doi.org/10.1051/0004-6361:20078344

A requirement for extra heating is indirectly stated by Luridiana et al. (1999) for NGC 2363.

A possible heating mechanism is conversion of mechanical energy provided by stellar winds and supernovae, although a conclusion of Luridiana et al. (2001) is not optimistic. A limitation of this mechanism is that most of this mechanical energy is likely to dissipate in hot, steadily expanding superbubbles (Martin 1996; Tenorio-Tagle et al. 2006). It is doubtful that heat conduction from this coronal gas could induce enough localized enhancement of T_e in the photoionized gas (e.g., Maciejewski et al. 1996), even though Slavin et al. (1993) suggest that turbulent mixing may favour an energy transfer. Martin (1997) suggests that shocks could help explain the trend of ionization throughout the diffuse interstellar gas of BCDs, but concedes that "shocks are only being invoked as a secondary signal in gas with very low surface brightness". Finally, photoelectric heating from dust is inefficient in metal-poor hot gas conditions (Bakes & Tielens 1994).

Nevertheless, the conclusion of SS99 is now accepted in many studies of GEHIIRs. It entails such far-reaching consequences concerning the physics of galaxies at large redshifts as to deserve close scrutiny. If, for exemple, the difference between observed and computed T_e([O III]) in the model by SS99 were to be accounted for by artificially raising the heat input proportionally to the photoionization heating, then the total heat input in the emitting gas should be doubled. *This problem therefore deals with the global energetics of the early universe.*

After reviewing previous models for I Zw 18 NW (Sect. 2), observations and new photoionization models are described in Sects. 3 and 4. Results presented in Sect. 5 are discussed in Sect. 6. Concluding remarks appear in Sect. 7. Models for other GEHIIRs are reviewed in Appendix A. Concepts undelying the new photoionization models are stated in Appendices B and C.

2. Photoionization models for I Zw 18 NW

Early models are reviewed by SS99. Dufour et al. (1988) envisioned a collection of small H II regions of different excitations. Campbell (1990) proposed to enhance r([O III]) by collisional quenching of [O III]λ 5007 in an ultra-compact structure (electron density $N_e = 10^5$ cm^{-3}). Stevenson et al. (1993) modelled a uniform sphere of radius ∼0.4″. Fairly satisfactory computed emission-line spectra were obtained, but the model H II regions were inacceptably compact according to subsequent imaging. Firstly, I Zw 18 NW is essentially an incomplete H II region shell of some 5″ in diameter surrounding a young MSC, which is not spatially coincident with the ionized gas. Secondly, both the highly T_e-sensitive line [O III]λ 4363 and the high-ionization line He IIλ 4686 are detected throughout the shell and beyond.

2.1. Recent modelling attempts

According to SS99, the "model" is a uniform, matter-bounded spherical shell whose only free parameter is a filling factor ϵ. The hydrogen density is $N_H = 10^2$ cm^{-3}, obtained by the electron density N_e([S II]) derived from the observed doublet intensity ratio r([S II]) = [S II]λ 6716/[S II]λ 6731. The central ionizing source is a synthetic stellar cluster which fits the observed continuum flux at 3327 Å and maximizes the nebular He II emission. The inner angular radius is 1.5″. The outer radius r_{out} is defined by the condition that the computed [O III]λ 5007/[O II]λ 3727 ratio fits the observed one. For increasing ϵ, the material is on average closer to the source and more ionized, which must be compensated for by increasing the optical depth to keep [O III]/[O II] constant, so that the computed Hβ flux increases and He II/Hβ decreases. For $\epsilon > 0.1$, the shell becomes radiation bounded, [O III]/[O II] grows larger than it should and r_{out} becomes less than the observed value (∼2.5″). Because of these trends, SS99 discard large-ϵ models and select a model with $\epsilon \sim 0.01$, on the basis that the computed r_{out}, Hβ and He II are roughly acceptable[1]. This "best model" presents two major drawbacks: (1) as stated by SS99, the computed r([O III]) is too small by a highly significant factor of 1.3, and (2) [S II] and [O I] are grossly underestimated.

2.2. The [OIII] line problem

Concerning r([O III]), SS99 note without justification that, for different values of N_H, "no acceptable solution is found". This is central in concluding that extra heating is required.

In response, Viegas (2002, hereafter V02) states that adopting a density less than 10^2 cm^{-3} (and $\epsilon = 1$) can help improve the computed r([O III]). However, in the example shown by V02 ($N_e = 30$ cm^{-3}), r([O III]) is still 10% low[2] and r([S II]) is not accurate. Moreover, not only [S II] and [O I], but now [O II] as well is strongly underpredicted, in accordance with the analysis of SS99. V02 then proposes that radiation-bounded filaments with density 10^4 cm^{-3} are embedded in the low-density gas at different distances from the source. If the emission of [S II] and [O I] (together with [O II]) can be increased in this way, this denser component has difficulties. Firstly, since the computed [O III]/[O II] ratio is not very much less than the observed one in these filaments, a sizeable fraction of [O III] must come from them (together with [O II]) and since, due to enhanced H I cooling (Appendix B.1), r([O III]) is now half the observed value, any composite model accounting simultaneously for [O III]λ 5007 and [O II]λ 3727 will underpredict r([O III]) in the same manner as the uniform model of SS99. Secondly, since at least half the [S II] emission should come from the filaments in which r([S II]) is again only half the observed value (large N_e), the composite r([S II]) will be inacceptably inaccurate. Thirdly, no explicit solution is found and it is unclear how a composite model of the kind envisaged by V02 will simultaneouly match all lines. From the evidence, the claim of V02 that "pure photoionization can explain I Zw 18 observations" is not supported. The inconclusiveness of the alternative she proposes effectively reinforces the standpoint of SS99.

2.3. The [OI] and [SII] line problem

[O I]λ 6300+63 is underpredicted by 2 dex in the model of SS99. Two configurations are envisaged by SS99.

2.3.1. Extremely dense filaments?

In a first configuration, radiation-bounded filaments of density 10^6 cm^{-3} are embedded in the H II region: the density is so high as to severely quench most lines other than [O I] and H I: only ∼10% of [S II]λ 6716+31 arises from these filaments,

[1] In this context, the Hβ and He II fluxes are poor selection criteria for ϵ, since the former is proportional to the (unknown) covering factor of the shell and the latter depends much on questionable synthetic stellar cluster spectra (Appendix C).

[2] The tolerance of 9% allowed by SS99 (adopted by V02) is probably too large (Sect. 3.3). This error bar is justified in the logic of SS99, who aim to demonstrate an absence of solution.

ensuring that r([S II]) is not much influenced. This attempt to solve in anticipation the problem met by V02 (Sect. 2.2) raises three difficulties, however: (1) condensations that contrast in density by a factor of 10^4 with their surroundings and present a large enough covering factor (∼10% according to SS99) as to intercept a significant fraction of the primary radiation would probably represent most of the mass; (2) since the main body of the model H II region produces only one quarter of the observed [S II]λ 6716+31 flux, it is not clear where this doublet would be emitted[3]; and (3) this highly artificial, strictly dual density distribution is not the schematic, first-approximation representation of some more complex reality, rather it is an essential feature of the model since any material at intermediate densities would usefully emit [S II]λ 6716+31, but lead to a totally wrong r([S II]), as in the description by V02.

2.3.2. Extremely distant filaments?

The second configuration proposed by SS99 involves radiation bounded "[O I] filaments" of density 10^2 cm^{-3}, located at ∼20″ from the source. If the spectroscopic objections of Sects. 2.2 and 2.3.1 are now removed since density is moderate and ionization is low in the filaments, new difficulties arise, notably with geometry: (1) the filaments observed at >10″ or more from the NW MSC of I Zw 18 have such a low surface brightness as to contribute negligibly to the brightness of the main shell (if they were projected upon it); (2) the spectrum of this weak emission up to ∼15″ – "Halo" of Vílchez & Iglesias-Páramo (1998), "Hα Arc" and "Loop" of Izotov et al. (2001a) – shows a flux ratio [O III]λ 5007/[O II]λ 3727 of order unity, whereas this ratio is 1/300 in the putative [O I] filaments, suggesting that the bulk of the emission observed at these distances arises from a gas whose density is much less than 10^2 cm^{-3}; (3) accepting all the same the existence of distant [O I] emitting regions, a very peculiar geometry would be required to project these regions precisely and uniquely upon the material of the irregular bright NW H II shell to be modelled; and (4) in projection, this shell appears as a 1.5−2.5″ "ring", which intercepts 1/200 of a 20″-radius sphere (including both the front and rear sides), incommensurable with the covering factor ∼1/10 assumed by SS99.

2.4. Previous models: conclusion

Attempts to model I Zw 18 fail to explain not only r([O III]) but the [O I] and [S II] lines as well. It is difficult to follow SS99 when they claim that they are "not too far from a completely satisfactory photoionization model" of I Zw 18. The explanatory value of their description is so loose as to jeopardize any inference drawn from it, including the requirement for extra heating in I Zw 18.

In Appendix A, a review of models obtained for other GEHIIRs reveals general trends and problems, which can be valuably analysed using the example of I Zw 18.

3. Observations of I Zw 18

3.1. Basic properties

Two bright regions 5″ apart, I Zw 18 NW and SE, correspond to two young MSCs associated with two distinct GEHIIRs, surrounded by a common irregular, filamentary halo of diffuse ionized gas (e.g., Izotov et al. 2001a), immersed in a radio H I 21 cm envelope rotating around the centre of mass located in between the GEHIIRs (e.g., van Zee et al. 1998). Although the H I column density peaks in the central region, large H I structures have no stellar counterparts. A fainter cluster, "Component C", deprived of massive stars (no prominent H II region), appears at 22″ to the NW of the main body. The two young MSCs, 1−5 Myr old, are the recent manifestations of a larger starburst, which started some 15 Myr ago in Component C and 20 Myr ago in the central region (Izotov & Thuan 2004, IT04). A 20−25 Myr age is consistent with the dynamics of the superbubble studied by Martin (1996). In a radio study, Hirashita & Hunt (2006) suggest 12−15 Myr. I Zw 18 is classified as a "passive BCD" (e.g., Hirashita & Hunt 2006), that is, the MSCs themselves are relatively diffuse, the stellar formation rate (SFR) is relatively low (Sect. 6.2) and the starburst is not instantaneous.

That a background population 300−500 Myr old may be the first generation of stars in this galaxy (Papaderos et al. 2002; IT04) is contested by Aloisi et al. (2007). The extended optical halo of I Zw 18 is mostly due to ionized gas emission. Unlike for usual BCDs, the bulk of the stars in I Zw 18 is highly concentrated, suggesting perhaps a young structure (Papaderos et al. 2002). The distance to I Zw 18, first quoted as 10 Mpc, has been revised to ∼13 Mpc (Östlin 2000) after correcting the Hubble flow for the attraction of the Virgo cluster. From AGB star magnitudes, IT04 obtain 14 ± 1.5 Mpc. At the distance D = 4.0×10^{25} cm (12.97 Mpc) adopted here, the diameter of the bright region I Zw 18 NW (5″) is over 300 pc. From new deep HST photometry revealing a red giant branch and Cepheid variables, Aloisi et al. (2007) obtain 18 ± 2 Mpc. Except for scaling, present results are just marginally changed if this larger distance is confirmed (Sect. 6.8).

3.2. Absolute HI line fluxes and reddening

According to Cannon et al. (2002, CSGD02), the absolute Hβ fluxes in the 5 polygons paving the NW region and the 7 polygons paving the SE region are 4.9 and 1.7 respectively in units of 10^{-14} erg cm^{-2} s^{-1}. Polygons NW D6 and SE D8 do not exactly belong to the main body of the H II regions and are dismissed. Tenuous emission around the polygons is also neglected.

The excess over the Case B recombination value of the observed average Hα/Hβ ratios, 2.94 and 2.97 in the NW and SE respectively, is attributed to dust reddening by CSGD02, who rightly doubt the large H I collisional excitation obtained by SS99 (Appendix D.1). It remains that the Balmer decrement is influenced by collisions and that the reddening correction to the observed spectrum of I Zw 18 has been overestimated. Collisional excitation results from a subtle anticorrelation between T_e and N(H^0)/N(H$^+$) within the nebula and can only be determined from a photoionization model (contrary to a statement by CSGD02, the maximum effect does not correspond to the hottest gas). The usually adopted recombination ratio is Hα/Hβ = 2.75 ± 0.01 (Izotov et al. 1999). It is anticipated that, according to present models (Sect. 5), a better Hα/Hβ is 2.83 ± 0.02. For use in the present study, published dereddened intensities (also corrected for stellar absorption lines) have been reddened by $\Delta E(B-V) = -0.04$ (in view of final results, a more nearly accurate correction could be $\Delta E(B-V) = -0.03$). Then the typical $E(B-V)$ for I Zw 18 NW shifts from 0.08 to 0.04, out of which the foreground Galactic contribution is about 0.02 (Schlegel et al. 1998). The reddening corrected Hβ fluxes for the main NW and SE H II regions are I(Hβ) = 5.6 and 2.0 respectively in units of 10^{-14} erg cm^{-2} s^{-1}.

[3] SS99 prefer casting doubt on the ionization balance of S$^+$.

In these units, the Hα flux is 33.0 over the central 13.7 × 10.5″ HST field (Hunter & Thronson 1995; CSGD02) and 42.0 over a 60 × 60″ field (Dufour & Hester 1990). Adopting overall averages Hα/Hβ = 2.8 and $E(B-V)$ = 0.06, the total dereddened Hβ flux for I Zw 18 is 18.3. Assuming that all of the ionizing photon sources belong to the bright NW and SE MSCs and that I Zw 18 is globally radiation bounded, the fraction of photons absorbed in the two main H II regions is 0.41. Let Q and $Q_{\rm abs}$ be respectively the number of photons (s^{-1}) emitted by the MSC and absorbed by the main shell of I Zw 18 NW alone. The fraction $Q_{\rm abs}/Q$ may be smaller than 0.41 for two reasons. Firstly, as expansion proceeds, the shells around the starbursts become more "porous" due to instabilities and the more evolved NW shell may be more affected. Assuming that no photons escape from the SE shell leads to a minimum $Q_{\rm abs}/Q$ = 0.34. A more realistic value is probably $Q_{\rm abs}/Q$ = 0.39 ± 0.02, since a complete absorption in the SE would result in a strong asymmetry of the diffuse halo, which is not observed. Secondly, photons may escape from I Zw 18. This effect is probably weak, given the amount and extension of H I in I Zw 18. The adopted nominal absorbed fraction for the NW shell will be $Q_{\rm abs}/Q$ = 0.37 ± 0.03, with 0.30 a conservative lower limit, obtained for a 25−30% escape from I Zw 18.

3.3. Spectroscopic observation summary

The optical spectrum of I Zw 18 has been observed for decades (Sargent & Searle 1970; Skillman & Kennicutt 1993, SK93; Legrand et al. 1997; Izotov et al. 1997a,b; Izotov & Thuan 1998; Vílchez & Iglesias-Páramo 1998, VI98; Izotov et al. 1999, ICF99; Izotov et al. 2001a; Thuan & Izotov 2005, TI05; Izotov et al. 2006a) with many instruments (HALE, KPNO, MMT, KECK, CFHT, etc.), the UV spectrum with IUE (Dufour et al. 1988) and HST (Garnett et al. 1997; Izotov & Thuan 1999, IT99), the IR spectrum with SPITZER (Wu et al. 2006, 2007), and the radio continuum with VLA (Hunt et al. 2005; Cannon et al. 2005).

The IUE aperture encompasses all of the bright regions. In addition to C III]λ 1909, there are indications for the presence of C IVλ 1549 and Si III]λ 1883+92. The HST spectrum allows a direct comparison of C III] with optical lines, but corresponds to such a limited area (0.86″) as to raise the question of the representativeness of the observation for I Zw 18 NW as a whole. Nonetheless, C III]/Hβ is identical within 10% in available measurements, once the re-evaluation of the Hα flux within the IUE aperture is taken into account (Dufour & Hester 1990).

The high-resolution mid-IR spectra of I Zw 18 (Wu et al. 2007, Wu07) are secured with a 4.7 × 11.3″ slit. Over the 13.7 × 10.5″ HST field, the de-redenned Hβ flux is 13.4, while the flux from strictly the two central H II regions, which fill only part of the SPITZER slit, is 7.6. The adopted Hβ flux corresponding to the mid-IR spectra is taken as 10 ± 1, the value also used by Dufour & Hester (1990) for the (partial) IUE aperture. Measuring line fluxes on the published tracings shows excellent agreement with tabulated values, except for [S III] 18.7μ, whose flux is tentatively shifted from 2.3 to 2.8 × 10^{-15} erg cm^{-2} s^{-1}. The UV and mid-IR spectra are not fully specific to I Zw 18 NW.

An average de-reddened emission line spectrum for I Zw 18 NW, close to the one secured by ICF99 in the optical range, is presented in Col. 2 ("Obs.") of Table 3 (line identifications in Col. 1; Cols. 3−6 are presented in Sect. 5). This spectrum differs little from those by Izotov & Thuan (1998) and SK93. A rather deep, high-resolution red spectrum is presented by SK93. A few weak lines are taken from a deep blue MMT spectrum by TI05, who however quote an [O II] 3727 flux larger than in earlier studies. Absolute fluxes for Hβ and the radio continuum are given on top of Table 3. The 21 cm and 3.6 cm fluxes, obtained from Cannon et al. (2005) as a sum of 3 contours for the NW shell, partly originate in non-thermal processes, not considered here. Line intensities are relative to Hβ = 1000. The intensity ratio [N II]λ 6584/λ 6548 quoted by SK93 is smaller than the theoretical value: this is presumably due to the presence of a broad Hα component (VI98). Correcting for the pseudo-continuum, the theoretical ratio is recovered and a new, smaller value is obtained for the sum of the [N II] doublet. [O II] 7320+30 (SK93) is uncertain and difficult to link to Hα. Taking into account weak (undetected) lines, such as [Ne IV]λ 4724, [Fe III]$\lambda\lambda$ 4702, 4734, 4755, a continuum slightly lower than the one adopted by TI05 leads to a moderate increase of the [Ar IV] line fluxes. Lines [Fe IV] 4906, [Fe II] 5158 and [Fe VI] 5176 are seen in the tracing by IT05, with tentative intensities 3, 2 and 2 (Hβ = 1000) respectively. Only [Fe IV] is considered in Table 3 (It is noted that the predicted intensities for these [Fe II] and [Fe VI] lines will be ∼1).

The most critical (de-reddened) line ratio is r([O III]) = 0.0246, the value also adopted by SS99. This is 3.1% larger than the often quoted value by SK93 (2″ slit), 0.6% smaller than the value by ICF99 (1.5″ slit) and 2.3% smaller than in the blue spectrum by TI05 (2″ slit).

4. New photoionization models for I Zw 18 NW

Models are computed using the standard photoionization code NEBU (Péquignot et al. 2001) in spherical symmetry with a central point-like source, suited to the apparent geometry of I Zw 18 NW since the bulk of the stars of the NW MSC belongs to a cavity surrounded by the GEHIIR shell. Radiation-bounded filaments embedded in a diffuse medium are modelled. The reader is referred to Appendices B and C for a perspective to the present approach. Atomic data are considered in Appendix D.

4.1. Stellar ionizing radiation

The central source Spectral Energy Distribution (SED) is treated analytically, with no precise reference to existing synthetic stellar cluster SEDs (Appendix C). No effort is made to describe the optical+UV continuum. The continuum flux at λ 3327 Å (de Mello et al. 1998) is not used to constrain the power of the MSC. Here, this constraint can be replaced to great advantage by the fraction of ionizing photons absorbed in the shell (Sect. 3.2).

The continuous distribution of stellar masses most often results in an approximately exponential decrease of flux with photon energy from 1 to 4 ryd in the SED of current synthetic MSCs (e.g., Luridiana et al. 2003). The sum of two black bodies at different temperatures can mimic this shape, yet provide flexibility to study the influence of the SED. The source of ionizing radiation is described as the sum of a hot black body, BB1 (temperature $T1 \geq 60$ kK; luminosity $L1$), and a cooler one, BB2 ($T2$ = 40−50 kK; $L2$). A constant scaling factor δ_4 (≤1), reminiscent of the discontinuity appearing in the SED of model stars (e.g., Leitherer et al. 1999) and constrained by the observed intensity of He IIλ 4686, is applied to the BB1 flux at ≥4 ryd. The ionizing continuum depends on five free parameters. The adopted $T2$ range is reminiscent of massive main sequence stars and lower $T2$s need not be considered. A sufficiently large range of $T1$ values should be considered, as the high-energy tail of the intrinsic SED is influenced by WR stars, whose properties are either uncertain or unknowable (Appendix C).

4.2. Ionized shell

The I Zw 18 NW shell extends from $R_i = 2.85 \times 10^{20}$ cm to $R_f = 4.75 \times 10^{20}$ cm (1.5″ and 2.5″ at $D = 4.0 \times 10^{25}$ cm).

In final complete models a smooth small-scale density distribution is assumed (gas filling factor ϵ unity). The gas density is defined by means of the following general law for a variable gas pressure P, given as a function of the radial optical depth, τ, at 13.6 eV:

$$P(\tau) = \frac{P_{out} + P_{in}}{2} + \frac{P_{out} - P_{in}}{\pi} \tan^{-1}\left[\kappa \log\left(\frac{\tau}{\tau_c}\right)\right]. \quad (1)$$

This law is a convenient tool to explore the effects of the density distribution on the model predictions. P is related to the pair of (T_e, N_H) via the ideal gas law, with T_e derived solving the statistical equilibrium equations at each step. At the first step of the computation ($\tau = 0$), the initial pressure is P_{in}, while at the last step ($\tau = \tau_m \sim \infty$) the final pressure is P_{out}. A smooth, rapid transition is obtained by adopting $\kappa = 30$ in all computations. Equation (1) introduces three free parameters: P_{in}, P_{out}, and the optical depth τ_c at which the transition from inner to outer pressure occurs. The picture of a filament core embedded in a dilute medium dictates that $P_{in} < P_{out}$. Each filament produces a radial shadow, which emits much less than the material in front of the filament and the filament itself, since it is only subject to the weak, very soft, diffuse field from the rest of the nebula. The shadows are neglected.

In order to represent radiation-bounded filaments embedded in a low density medium (Appendix B.1), at least two sectors are needed: a "Sector 1" with $\tau_m \gg \tau_c$ (radial directions crossing a filament) and a "Sector 2" with $\tau_m < \tau_c$. To first order, only two sectors are considered. Observation shows that the He II emission, although definitely extended, is relatively weaker in the filaments surrounding the main shell (VI98; Izotov et al. 2001a). This deficit of He II, unrelated to an outward decrease of the ionization parameter since He II is a pure "photon counting" line above 4 ryd, suggests instead that in no radial direction is the main shell totally deprived of absorbing gas. With the concern of reaching a more significant description, the same small $\tau_m(3) = 0.05$ will be attached to the remaining "Sector 3" required to make up the covering factor of the source to unity in all complete models. The emission of Sector 3, a moderate contribution to the He II intensity, does not impact on conclusions concerning the main shell and the source.

For simplicity, in any given run, the values of the three defining parameters of Eq. (1) are assumed to be shared by all three sectors. Note that τ_c and P_{out} act only in Sector 1. The topology (Appendix B.2) of the model shell is determined by giving in addition the covering factors f_1^{cov} of Sector 1 (radiation-bounded) and f_2^{cov} of Sector 2 (matter-bounded), with the condition:

$$f_3^{cov} = 1 - (f_1^{cov} + f_2^{cov}) > 0, \quad (2)$$

and finally the optical depth $\tau_m(2)$ ($<\tau_c$) of Sector 2. The full model shell structure depends on six free parameters.

Adopting the same R_i and the same parameters for $P(\tau)$ in the three sectors and assuming that the outer radius of Sector 1 is R_f make the computed outer radii of other sectors smaller than R_f. If, however, one would like Sector 2 to extend up to R_f and perhaps beyond, models should be re-run for this sector using a $P(\tau)$ with $P_{out}(2) < P_{in}$ and $\tau_c < 1$. No significant consequences for the computed spectrum result from this change, as the increase of radius and the decrease of density in the outermost layers of Sector 2 (say, $\tau \sim 1$) have opposite effects on the "local" ionization. Also, "improving" the artificial geometry of Sector 3 (a thin shell at radius R_i) by assuming a lower $P_{in}(3)$ or else a filling $\epsilon \ll 1$ would not change the intensity of He II at all, while the emission of other lines from this sector is negligible.

Although three sectors are considered, Sector 3 is of no practical consequence for the main shell and no parameter is attached to it. A model based on the above description will be termed a "two-sector model" (Sect. 5.3).

Table 1. Constraints on model parameters[a].

Parameter	Constraints
$E(B-V)$	Hα/Hβ; (No freedom: $E(B-V) = 0.04$)
R_i	No freedom $R_i = 2.85 \times 10^{20}$ cm
f^{cov}	Absolute $I(H\beta) = 5.6 \times 10^{-14}$ erg cm^{-2} s^{-1}
$L1$, $L2$	Cluster SED; $f^{cov} \leq 1.0$; $Q_{abs}/Q \sim 0.37$
$T1$, $T2$	$\delta_4 \leq 1.0$; ($\log(Q_{He}/Q) \sim -0.5$)
δ_4	He IIλ 4686
He	He/H = 0.08; He Iλ 5876?
C	C III]λ 1909
N	[N II]λ 6584
O	[O III]λ 5007
Ne	[Ne III]λ 3869
Mg	Mg/Ar = 10.; Mg I]λ 4571?
Al	Al/Ar = 1.; Al IIIλ 1855?
Si	Si/Ar = 10.; Si III]λ 1883?
S	S/Ar = 4.37; $\langle$[S III]$\rangle$?
Ar	[Ar III]λ 7135
Fe	[Fe III]λ 4658
One-component constant density run ($N0$, $N1$):	
N_H	r([S II]) = [S II]λ 6716/[S II]λ 6731 ($\pm$)
τ_m	[O II]λ 3727
ϵ	$R_f = 4.75 \times 10^{20}$ cm
One-component model with Eq. (1) ($M1$):	
$\epsilon = 1.0$	No freedom
P_{out}	r([S II])
τ_c	[O II]λ 3727
P_{in}	$R_f = 4.75 \times 10^{20}$ cm
Two-component model ($M2$, $M3$, $M4$) added freedoms:	
f_1^{cov}	$f_2^{cov} > 0$; $f^{cov} = f_1^{cov} + f_2^{cov} < 1$
f_2^{cov}	$\tau_m(2) < \tau_c$; global 3D geometry
$\tau_m(2)$	Fine tuning $I(H\beta)$ for given f_i^{cov}

[a] Question marks attached to dismissed constraints (see text).

4.3. Model parameters and constraints

Correspondances between model parameters and constraints are outlined in Table 1. The parameters are interrelated and iterations are needed to converge to a solution. The weak dependance of $E(B-V)$ on the model Balmer decrement (Sect. 3.2) is neglected. The SED is not fully determined by the major constraint Q_{abs}/Q. Other constraints are in the form of inequalities, some are semi-quantitative or deal with "plausibility" arguments.

One emission line is selected to constrain each elemental abundance. In Table 1, a question mark is appended to those lines with unreliable intensities (Table 3): the intensity of Mg I]λ 4571+62 is given as an upper limit as the lines are barely detected (TI05) and suspected to be blended with a WR feature (Guseva et al. 2000); detection of Al IIIλ 1855 is an estimate from a tracing of the HST spectrum; Si III]λ 1883+92 is barely seen in the IUE spectrum and only the first component of the doublet is detected in the HST spectrum (IT99). The abundances of Mg, Al and Si are arbitrarily linked to that of argon (Table 1), assuming abundance ratios close to solar (Lodders 2003). For simplicity, the solar S/Ar ratio is also adopted and the computed sulfur line intensities can be used to scale S/H according to any

preferred criterion (Sect. 6.7). He I emission lines are blended with strong stellar absorption lines (ICF99). He/H is set at 0.08 by number.

In the lower part of Table 1 we give observational constraints for the structural parameters of the shell, depending on assumptions. In preliminary constant-density "runs" (*N*0, *N*1, not genuine models; Sect. 5.1), a generalization of the approach of SS99 (Sect. 2.1) is adopted. A one-component model (*M*1; Sect. 5.2) shows the influence of Eq. (1). Two-component models (*M*2, *M*3 and *M*4; Sect. 5.3) generalize *M*1 according to Sect. 4.2.

5. Results

Input and output model properties are listed in the first column of Table 2 as: (1) five primary ionizing source parameters (Sect. 4.1); (2) resulting numbers of photons (s^{-1}) Q and Q_{He} emitted by the source above 13.6 and 24.6 eV respectively; (3) four (*N*0, *N*1, *M*1) to six (*M*2, *M*3, *M*4) shell parameters (Sect. 4.2); (4) elemental abundances; (5) photon fraction Q_{abs}/Q absorbed in the shell; (6) mass M_{gas} of ionized gas in units of $10^6\ M_\odot$; (7) mean ionic fractions of H^+ and oxygen ions weighted by N_e; (8) average T_e and t^2 weighted by $N_e \times N_{ion}$ and average N_e weighted by N_{ion} for H^+ and oxygen ions.

The model SEDs (Sect. 4.1) are shown in Fig. 1: panel (a) is common to *N*0, *N*1 and *M*1; panels (b), (c) and (d) correspond to *M*2, *M*3 and *M*4 respectively. Radiation is harder and stronger in panel (a) (see "hardness coefficient" α in caption to Fig. 1). The gas pressure laws $P(\tau)$, drawn in Fig. 2 (parameters in Table 2), illustrate the contrast between preliminary runs and adopted models.

Line identifications and observed de-reddened intensities are provided in Cols. 1 and 2 of Table 3. Computed intensities appear in Cols. 3 and 5 for Run *N*0 and Model *M*2 respectively. Predictions are given for some unobserved lines (intensities are 10 times the quoted values for H I 1215 Å and $2h\nu$). The ratios of computed to observed intensities, noted "*N*0/O" and "*M*2/O", appear in Cols. 4 and 6 for *N*0 and *M*2 respectively. Ideally, these ratios should be 1.00 for all observed lines.

Inasmuch as the convergence is completed, at least all lines used as model constraints (Table 1) must be exactly matched by construction (Table 3). To evaluate the models, these lines are therefore useless. Similarly, "redundent" lines (H I and He I series, etc.), which carry no astrophysically significant information in this context, as well as unobserved lines, can be discarded. Remaining "useful" lines are listed in Cols. 1, 2 of Table 4 and model intensities divided by observed intensities in Cols. 3–8 for *N*0–*N*1, *M*1–*M*4 respectively. These intensities are "predictions" in that they are not considered at any step of the convergence. In Table 4[4], [O III]λ4363 Å stands out as the strongest, most accurately measured optical line. Q_{abs}/Q is repeated in Table 4.

Table 2. I Zw 18 NW: model parameters and properties.

Parameters of model	Run[a] N0–N1 2–3	Model[b] M1 4	M2 5	M3 6	M4 7
Central source parameters					
$T1/10^4$ K	10.	10.	8.	8.	12.
$L1/10^{41}$ erg s^{-1}	3.5–1.6	3.5	2.0	1.6	1.25
δ_4	.12–.67	0.73	0.83	0.93	0.24
$T2/10^4$ K	4.	4.	4.	5.	4.
$L2/10^{41}$ erg s^{-1}	3.5–1.6	3.5	2.0	1.6	2.5
$\log(Q) - 51.$	1.04–.71	1.054	0.829	0.779	0.734
$-\log(Q_{He}/Q)$	.462–.447	0.445	0.523	0.493	0.539
Ionized shell parameters					
ϵ	.0042–.31	1.00	1.00	1.00	1.00
$P_{in}/k/10^5$CGS	38.–8.3	5.01	3.40	2.96	2.71
$P_{out}/k/10^5$CGS	–	23.2	21.7	25.4	26.8
τ_c	–	5.7	4.9	4.0	4.3
f_1^{cov}	1.–0.43	0.20	0.26	0.23	0.29
f_2^{cov}	–	–	0.30	0.50	0.60
τ_m or $\tau_m(2)$	.96–300.	270.	1.21	1.46	1.00
Elemental abundances by number (H = 10^7)					
C	60–52	45.8	38.8	35.3	47.4
N	8.1–5.3	3.9	4.1	4.0	3.8
O	198–192	172.	168.	162.	173.
Ne	33–30	26.4	25.7	24.8	26.9
S (Table 1)	3.4–3.9	5.0	4.3	4.3	5.0
Ar	.77–.90	1.14	0.99	0.98	1.13
Fe	4.8–5.8	5.8	6.1	6.0	6.5
Mean shell properties weighted by $N_e \times N_{ion}$, except for N_e					
Q_{abs}/Q	.20–.43	.200	.343	.380	.426
$M_{gas}/10^6\ M_\odot$	.15–.92	1.02	1.52	1.74	1.79
H^+/H	.998–.98	.957	.961	.963	.948
O^0/O	.00–.017	.041	.038	.037	.052
O^+/O	.076–.10	.122	.125	.129	.131
O^{2+}/O	.910–.85	.784	.793	.790	.773
O^{3+}/O	.014–.03	.049	.043	.043	.042
$T_e(H^+)/10^4$ K	1.65–1.73	1.873	1.859	1.896	1.839
$T_e(O^0)/10^4$ K	1.61–1.14	1.040	1.013	1.012	1.003
$T_e(O^+)/10^4$ K	1.63–1.43	1.320	1.315	1.309	1.272
$T_e(O^{2+})/10^4$ K	1.66–1.75	1.911	1.915	1.961	1.898
$T_e(O^{3+})/10^4$ K	1.76–2.1	2.576	2.402	2.449	2.479
$N_e(H^+)/$ cm^{-3}	99–18	17.3	11.1	9.8	9.4
$N_e(O^0)/$ cm^{-3}	99–8.5	46.7	34.0	37.8	41.1
$N_e(O^+)/$ cm^{-3}	99–16	62.7	48.0	54.0	54.8
$N_e(O^{2+})/$ cm^{-3}	99–18	15.4	10.2	8.9	8.5
$N_e(O^{3+})/$ cm^{-3}	100–19	10.1	7.4	6.3	5.7
$t^2(H^+)$	.002–.014	.032	.026	.028	.030
$t^2(O^0)$	.001–.018	.022	.024	.023	.020
$t^2(O^+)$	.0013–.02	.021	.024	.024	.023
$t^2(O^{2+})$	.002–.008	.013	.010	.010	.010
$t^2(O^{3+})$	.0010–05	.0008	.0006	.0007	.0016

[a] Constant N_H. *N*0: $N_H = 92$ cm^{-3}; *N*1: $N_H = 17.0$ cm^{-3}.
[b] N_H from thermal pressure of Eq. (1).

5.1. Constant density runs with filling factor: N0, N1

*N*0 is a preliminary run (Col. 2 of Table 2) in which N_H is constant and Q, Q_{He}, R_i and R_f are as in the description by SS99 (corrected for the larger D). The convergence process, involving O/H, Ne/H, etc. (Table 1), is more complete than the one performed by SS99, but the differences in procedures do not change the conclusions. If N_H is in principle derived from r([S II]), the sensitivity of r([S II]) to N_e is relatively weak at the low density prevailing in the shell, while the exact value adopted for N_H may, in this particular structure, strongly influence the computed spectrum. By coherently changing N_H, ϵ and f^{cov}, the three constraints $I(H\beta)$, [O III]/[O II] and R_f can be fulfilled along a sequence. *N*0 is extracted from this sequence by assuming, as in the SS99 run, a covering factor $f^{cov} = 1$. The solution is close to the one chosen by SS99, with $N_H = 92$ cm^{-3}, $\epsilon = 0.0042$, (radial) $\tau \sim 1$ ($\equiv\tau_m(2)$ in Table 2) and r([S II]) only −2.1% off the observed value. *N*0 (Cols. 3, 4 of Table 3; Col. 3 of

[4] Since [O III]λ5007+4959 is exactly matched, the entry [O III]λ4363 in Tables 4 and 5 is the "normalized r([O III])", i.e., the ratio of the computed r([O III]) to the observed r([O III]).

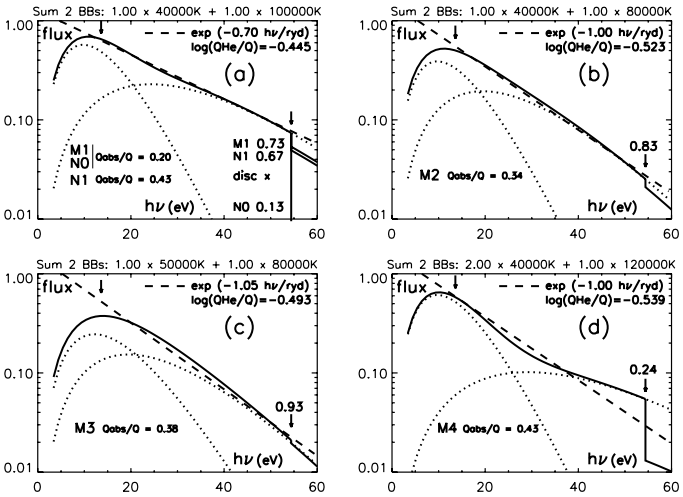

Fig. 1. Spectral energy distribution (SED) for I Zw 18 NW models. Flux in erg s^{-1} eV^{-1} multiplied by an arbitrary constant versus photon energy $h\nu$ in eV. The SED (solid line) is the sum of two black bodies (dotted lines), with a discontinuity at 4 ryd (Sect. 4.1). Panel **a)** is common to $N0$, $N1$ and $M1$. Panels **b)**, **c)** and **d)** correspond to $M2$, $M3$ and $M4$ respectively. Vertical arrows appear at 1 and 4 ryd. Straight dashed lines of the form $\exp(-\alpha\, h\nu/\mathrm{ryd})$ are exponential approximations of the SEDs over the range 1−4 ryd. The exponential expressions are written in the panels corresponding to the SEDs (α = 0.70, 1.00, 1.05 and 1.00 in panels **a)** to **d)**, with α a measure of the EUV continuum hardness). Some of the SED data provided in Table 2 ($Q_{\rm He}/Q$, discontinuity factor δ_4 and $Q_{\rm abs}/Q$) are recalled in the panels.

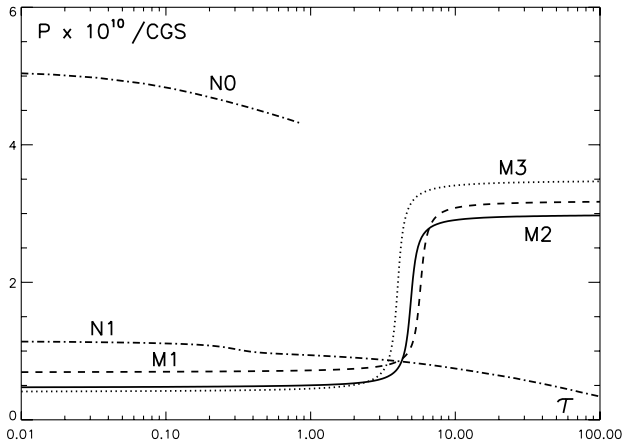

Fig. 2. Gas pressure versus optical depth τ for models $M1$ (dashed line), $M2$ (solid line) and $M3$ (dotted line), governed by Eq. (1) with parameters in Table 2. $M4$, close to $M3$, is not shown. For comparison, the dash-dotted lines correspond to the constant density runs $N0$ and $N1$.

Table 4) confirms the problems met in SS99 with [O III]λ 4363 and [O I]λ 6300 (Sect. 2.1).

$N0$ also fails in that $Q_{\rm abs}/Q$ is half the expected value. Decreasing Q (SED luminosity) implies to decrease $N_{\rm H}$ (for [O III]/[O II]) and increase ϵ (for $I(\mathrm{H}\beta)$). Decreasing $N_{\rm H}$ should help increase $T_{\rm e}$, thus r([O III]), and the high ionization lines, largely underestimated in $N0$. Correlatively, [O III]/[O II] is restored for a larger $\tau_{\rm m}$, which helps increase [O I] and other low-ionization lines. By further decreasing $N_{\rm H}$ and increasing ϵ, whilst fine-tuning $f^{\rm cov}$ to keep the outer shell radius $R_{\rm f}$ (and $I(\mathrm{H}\beta)$) and δ_4 (for He II), it is possible to further increase $\tau_{\rm m}$ until the shell becomes radiation bounded. The resulting (unique) solution is $N1$ (Col. 3 of Table 2; Col. 4 of Table 4), which improves upon $N0$ concerning [O I] and high-ionization lines, while $Q_{\rm abs}/Q \equiv f^{\rm cov} = 0.43$ is slightly too large. Because of the

Table 3. Model outputs for I Zw 18 NW: $N0$ and $M2$.

Line id./Models	Obs.	N0	N0/O	M2	M2/O
Absolute fluxes ($I(\mathrm{H}\beta)$ in 10^{-14} erg cm^{-2} s^{-1})					
$I(\mathrm{H}\beta)$	5.6	5.6	1.00	5.6	1.00
1.43 GHz /mJy	0.433	0.240	0.55	0.256	0.59
8.45 GHz /mJy	0.286	0.202	0.71	0.216	0.76
Relative line fluxes (wavelengths in Å or μm)					
H I 4861	1000.	1000.	1.00	1000.	1.00
H I 6563	2860.	2840.	0.99	2830.	0.99
H I 4340	461.	473.	1.03	473.	1.03
H I 4102	266.	267.	1.00	267.	1.00
H I 1215 (/10)	–	2950.	–	3010.	–
H I 2$h\nu$ (/10)	–	1550.	–	1620.	–
He I 3888	90.4	89.6	0.99	90.5	1.00
He I 4471	21.4	34.9	1.63	35.2	1.64
He I 5876	67.7	92.0	1.36	91.3	1.35
He I 6678	25.3	25.3	1.00	25.6	1.01
He I 7065	24.4	23.4	0.96	22.9	0.94
He I 10830	–	251.	–	190.	–
He II 4686	36.8	36.8	1.00	36.8	1.00
C III] 1909+07	467.	467.	1.00	467.	1.00
Si III] 1882+92	270.:	229.	0.85	340.	1.26
Al III 1855+63	111.:	42.9	0.39	82.9	0.75
O III] 1664	<230	127.	>.5	208.	>.9
C IV 1549	510.:	74.2	0.14	334.	0.65
Si IV 1397 }[a]	<300	22.7	>.1	127.	>.5
O IV] 1398 }	*	2.0	*	24.9	*
[N II] 6584+48	9.2	9.2	1.00	9.2	1.00
[O I] 6300+63	8.5	0.12	0.01	8.6	1.01
[O II] 3726+29	238.	238.	1.00	238.	1.00
[O II] 7320+30	6.3:	9.5	1.50	7.5	1.18
[O III] 5007+..	2683.	2680.	1.00	2680.	1.00
[O III] 4363	65.9	47.8	0.73	63.2	0.96
[O III] 51.8 μm	–	174.	–	137.	–
[O III] 88.3 μm	–	216.	–	213.	–
[O IV] 25.9 μm	49.1	18.2	0.37	47.8	0.97
[Ne II] 12.8 μm	9.0:	1.3	0.14	1.9	0.21
[Ne III] 3868+..	191.	191.	1.00	191.	1.00
[Ne III] 15.5 μm	45.7	60.0	1.31	48.9	1.07
Mg I] 4571+62	<3.0	1.5	>.5	1.2	>.4
[Si II] 34.8 μm	157.	4.7	0.03	22.0	0.14
[S II] 6716	22.5	6.7	0.30	17.6	0.78
[S II] 6731	16.9	5.1	0.30	13.1	0.78
[S II] 4068 }	3.7	1.1	0.41	2.2	0.99
[Fe V] 4071 }	*	0.4	*	1.5	*
[S III] 9531+..	114.	130.	1.15	113.	0.99
[S III] 6312	6.7	6.0	0.89	5.7	0.85
[S III] 18.7 μm	28.0	32.2	1.15	26.2	0.95
[S III] 33.5 μm	120.	54.5	0.45	48.0	0.40
[S IV] 10.5 μm	48.0	41.7	0.87	92.6	1.93
[Ar III] 7136+..	23.5	23.5	1.00	23.5	1.00
[Ar III] 8.99 μm	–	8.6	–	8.1	–
[Ar IV] 4711 }	8.6	1.5	0.76	8.2	1.53
He I 4713 }	*	5.0	*	5.0	*
[Ar IV] 4740	4.5	1.2	0.26	6.2	1.39
[Fe II] 5.34 μm	–	0.1	–	10.8	–
[Fe II] 26.0 μm	34.	0.0	0.00	3.4	0.10
[Fe III] 4658	4.5	4.5	1.00	4.5	1.00
[Fe III] 4986	7.4	5.8	0.78	7.0	0.94
[Fe III] 22.9 μm	–	2.2	–	3.2	–
[Fe IV] 4906	3.0:	1.6	0.54	3.1	1.02
[Fe V] 4227	1.8	1.5	0.84	5.5	3.10

[a] In Col. 1, blends are indicated by braces. The observed intensity of a blend is attributed to the first line and an asterisk to the second line.

Table 4. Model "predictions" for I Zw 18 NW: model intensities divided by observed intensities.

Line ident.	Obs.	N0–N1	M1	M2	M3	M4
	2	3 – 4	5	6	7	8
Q_{abs}/Q^a	0.37	.20–.43	0.20	0.34	0.38	0.43
C IV 1549	500:	.14–.41	1.12	0.65	0.64	1.08
[O I] 6300+	8.5	.01–.59	1.19	1.01	0.95	1.38
[O II] 7320+	6.3:	1.5–1.24	1.19	1.18	1.19	1.15
[O III] 4363	65.9	.73–.82	0.96	0.96	1.00	0.94
[O IV] 25.9μ	49.1	.37–.84	1.08	0.97	0.94	0.98
[Ne II] 12.8μ	9.0:	.14–.10	0.14	0.21	0.22	0.23
[Ne III]15.5μ	45.7	1.31–1.22	1.09	1.07	1.02	1.11
[Si II] 34.8μ	157.	.03–.10	0.17	0.14	0.14	0.18
Si III] 1882+	270:	.85–.99	1.12	1.26	1.34	1.16
[S II] 6716	22.5	.30–.54	0.96	0.78	0.77	1.10
[S II] 6731	16.9	.30–.51	0.96	0.78	0.77	1.10
[S II] 4068^b	3.7^b	.30–.43	0.73	0.58	0.58	0.80
[S III] 9531+	114.	1.15–1.05	0.95	0.99	1.00	0.92
[S III] 6312	6.7	.89–.84	0.77	0.85	0.87	0.75
[S III] 18.7μ	28.	1.15–1.01	0.94	0.95	0.94	0.91
[S III] 33.5μ	120.	.45–.44	0.39	0.40	0.40	0.39
[S IV] 10.5μ	48.	.87–1.50	2.15	1.93	1.97	2.15
[Ar IV] 4740	4.5	.26–.73	1.87	1.39	1.47	1.76
[Fe II] 26.0μ	34.	.00–.05	0.10	0.10	0.10	0.14
[Fe III] 4986	7.4	.78–1.15	0.90	0.94	0.89	0.89
[Fe IV] 4906	3.0:	.54–.70	0.96	1.02	1.09	1.02
[Fe V] 4227	1.8:	.84–2.3	2.1	3.1	3.2	3.1

[a] Q_{abs}/Q: absolute values.
[b] λ 4068 intensity not corrected for [Fe V]λ 4071 (Table 3).

much lower density, N_H = 17 cm^{-3}, the ratio r([S II]) is now +4.7% off, worse than in $N0$, yet not decisively inacceptable. Nevertheless, the normalized r([O III]), enhanced from 0.73 to 0.82, is still significantly too small. This failure of $N1$ is illustrated in the upper panels of Figs. 3–5. The runs of N_e and T_e with nebular radius R are shown in Figs. 3a, 4a for $N0$ and Figs. 3b, 4b for $N1$. Ionic fractions of oxygen versus τ are shown in Figs. 5a and 5b for $N0$ and $N1$ respectively. In $N0$, T_e is above 1.55×10^4 K everywhere. In $N1$, the inner T_e is 3800 K higher than in $N0$, but O^{2+} is abundant up to $\tau = 15$, where T_e is below 1.40×10^4 K and the average T_e([O III]) is not much increased.

This generalization shows that no solution with constant N_H exists even for the rather hard SED adopted by SS99. In an extreme variant of $N1$, the SED is just one 10^5 K black body (converged $L = 2.7 \times 10^{41}$ erg s^{-1}, $\delta_4 = 0.41$, $\log(Q_{He}/Q) = -0.27$), but the normalized r([O III]) = 0.87 is still too small, despite the unrealistically hard SED.

5.2. A one-sector photoionization model: M1

Model $M1$ includes the same primary source as Run $N0$ and again only one sector, but with N_H controlled by Eq. (1) (Fig. 2). Parameters appear in Col. 4 of Table 2 and predictions in Col. 5 of Table 4. The lines [O III]λ 4363 and [O I]λ 6300 are improved compared to Run $N0$ (and even $N1$), as are [S II] and [O IV].

The decisive merit of Model $M1$ is to demonstrate that, with no extra free parameter, no change of shell size and no significant change of source SED, *the "r([O III]) problem" met in N0 can be solved* by considering radiation-bounded filaments embedded in a lower density (higher ionization) medium instead of a clumped shell at constant density. While the normalized r([O III]) is 0.96 ([O III] in Table 4), no dense or distant clumps of the kind postulated by SS99 (Sect. 2) are needed to account for low-ionization lines. The pressure contrast is <5.

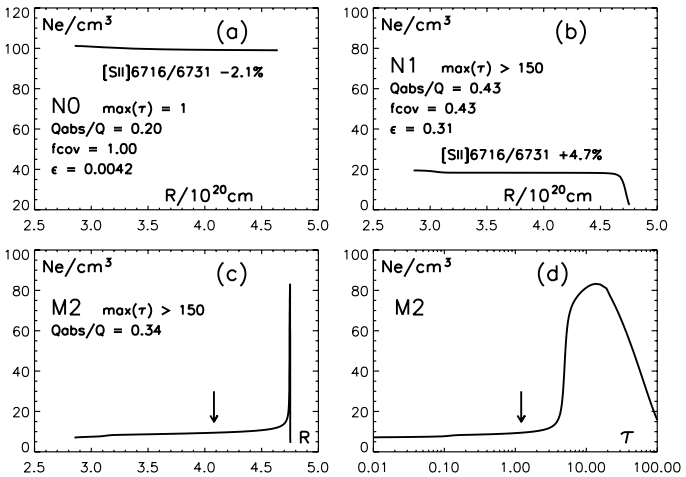

Fig. 3. Local electron density N_e versus shell radius R in I Zw 18 NW models: **a)** $N0$, **b)** $N1$, **c)** $M2$; and versus optical depth τ at 1 ryd: **d)** $M2$. In panels **c)** and **d)**, the vertical arrows indicate the boundary of the matter-bounded sector 2 of Model $M2$. Also provided are the optical thickness "max(τ)" (">150" means "radiation bounded"), the fraction of primary photons absorbed Q_{abs}/Q, and, where relevant ($N0$ and $N1$), the covering factor f^{cov}, the filling factor ϵ and the departure of the computed [S II] doublet ratio from observation in %.

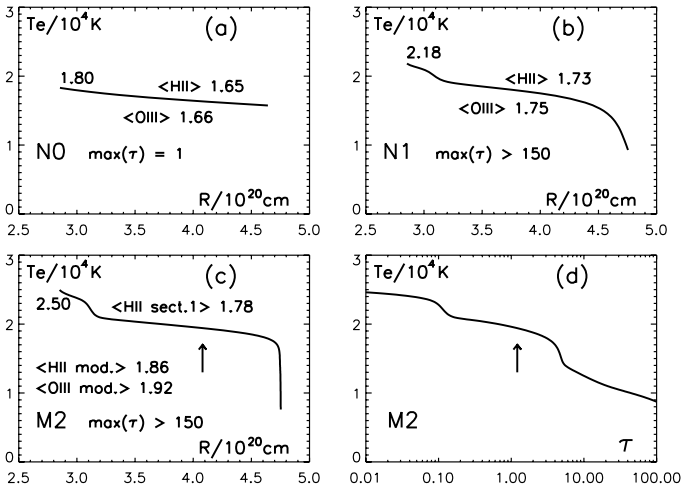

Fig. 4. As in Fig. 3 for local electron temperature $T_e/10^4$ K. The maximum T_e and average T_e's weighted by $N_e \times N(H^+)$ and by $N_e \times N(O^{2+})$ are noted along each curve. In panel **c)**, $\langle T_e \rangle$ is given for both the radiation bounded sector ($\langle$sect.1$\rangle$) and the full model $M2$ ($\langle$mod.$\rangle$).

Q_{abs}/Q is again too small, but Q cannot decrease because δ_4 is close to unity (Table 2). In $N0$, δ_4 was (perhaps anomalously) small, enabling a shift from $N0$ to $N1$. Hardening the already hard primary ($\alpha = 0.7$ due to large $T1$; Fig. 1) would enhance [Ar IV], predicted too strong. Also, f^{cov} is only 0.20, resulting in an artificial cigar-like radial distribution, in which the low-density gas exactly shields the denser filaments from direct primary radiation.

Obviously, the limits of the one-sector model are being reached. A matter-bounded sector is to be added for the sake of a larger absorbed fraction of photons in the shell, but not principally to improve the already quite satisfactory intensities of [O III]λ 4363 and [O I]λ 6300.

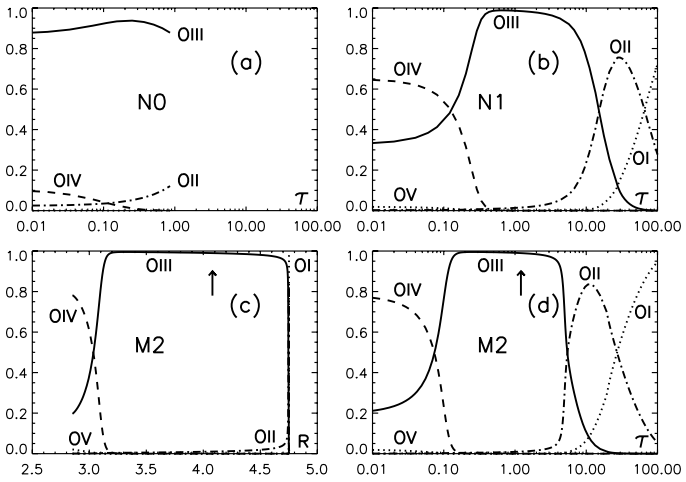

Fig. 5. Local fractional concentrations of O^0 (dotted line), O^+ (dot-dashed line), O^{2+} (solid line), O^{3+} (dashed line) and O^{4+} (dotted line again) versus τ in I Zw 18 NW models: **a)** *N*0, **b)** *N*1, **d)** *M*2; and versus *R*: **c)** *M*2. Vertical arrows as in Fig. 3.

Table 5. Influence of shell parameters on selected line intensity predictions for models *M*2 and *M*4.

Param./line	M2	M2b	M2c	M4b	M4	M4c
	2	3	4	5	6	7
f_1^{cov}	0.26	0.26	0.22	0.29	0.29	0.22
f_2^{cov}	0.30	0.60	0.60	0.30	0.60	0.60
$\tau_m(2)$	1.21	0.62	0.92	2.17	1.01	1.57
τ_c	4.9	4.7	3.8	4.6	4.3	3.0
$P_{in}/k/10^5$	3.4	3.4	3.1	2.7	2.7	2.4
$P_{out}/k/10^5$	21.7	22.5	24.6	26.8	26.8	26.8
O/H×10^7	168.	165.	162.	178.	173.	171.
[O I] 6300+	1.01	1.00	0.92	1.42	1.37	1.06
[O III] 4363	0.96	0.97	1.00	0.92	0.94	0.95
[O IV] 25.9μ	0.97	0.91	0.92	1.05	0.98	0.99
[S II] 6716	0.78	0.81	0.79	1.05	1.10	0.84
[S IV] 10.5μ	1.93	1.97	2.05	2.07	2.15	1.92
[Ar IV] 4740	1.39	1.48	1.62	1.55	1.77	1.81

5.3. Two-sector photoionization models: M2, M3, M4

The enhancement of He II and [O III] related to the matter-bounded sector must be balanced by a weaker/softer SED. Models illustrate the influence of the SED (Fig. 1).

Given a SED and both covering factors, then $\tau_m(2)$, τ_c and δ_4 can be fine-tuned to account for $I(H\beta)$, [O III]/[O II] and He II. Iterations along the same lines as for Model *M*1 eventually lead to a model, provided that the limits on parameters are respected (Table 1). A two-parameter model sequence can be attached to any SED by considering several pairs (f_1^{cov}, f_2^{cov}), but little freedom is attached to f_1^{cov}, as Sector 1 is where ∼75% of Hβ and most of [O II] come from. Then f_1^{cov} must be of the order of, or moderately larger than the f^{cov} of the one-sector model, say, in the range 0.2−0.3. Also f_2^{cov} cannot be small since one-sector models are rejected (Sect. 5.2) and $f_1^{cov} + f_2^{cov}$ must be kept significantly less than unity to enable He II excitation beyond the shell (Sect. 4.2), implying $f_2^{cov} \sim 0.3-0.6$.

5.3.1. Model *M2* and variants

Model *M*2 (Col. 5 of Table 2) is the first "complete" model. Q_{abs}/Q is at the low end of the nominal interval. Ouput of line intensities (Cols. 5−6 of Table 3; Col. 6 of Table 4) is to be contrasted to the *N*0 output. Runs of N_e and T_e with *R* are shown in Figs. 3c, 4c. The sharp "spike" of the N_e curve shows how thin a radiation-bounded filament is compared to the shell. Runs of N_e and T_e are best seen in plots versus τ (Figs. 3d, 4d). In plots for *M*2, vertical arrows mark the outer boundary of Sector 2. Ion fractions O^{n+}/O versus *R* and τ are shown in Figs. 5c,d.

Sufficient ionization is maintained in *M*2 due to the lower average density, which also helps increase T_e in the high-ionization layers, despite the significantly softer radiation field (smaller Q_{He}/Q and larger α, Fig. 1b): the inner T_e is now 2.5×10^4 K. In Fig. 4d, the jumps of T_e at $\tau \sim 0.1$ and ∼4.7 correspond to the boundaries of the He^{2+} shell (fairly well traced by O^{3+} in Fig. 5d) and the filament respectively. Comparing Fig. 5d to Fig. 5b, the ionic fractions are qualitatively similar in Model *M*2 and Run *N*1, but the transition from O^{2+} to O^+ is sharper and occurs at a smaller optical depth in *M*2.

Average properties and abundances of Model *M*2 are similar to those of *M*1 and the predicted [O III]λ 4363 intensity is again slightly weak, although the score of *M*2 is significantly better for [Ar IV] and [S IV] (Col. 6 of Table 4).

Variants to Model *M*2 can be obtained by changing f_1^{cov} and f_2^{cov} within limits, while retaining source parameters (except for minute fine-tuning of δ_4). In Col. 1 of Table 5 are listed 7 shell parameters and 6 lines extracted from Table 4. *M*2 (Col. 2 of Table 5) is compared to models *M*2*b* (Col. 3) and *M*2*c* (Col. 4). Increasing f_2^{cov} from a small to a large value, with f_1^{cov} left unchanged, structure parameters are not much changed except for a decrease of $\tau_m(2)$ and a small decrease of O/H due to the larger weight of the hot high-ionization zone. Accordingly, [Ar IV] is increased, but [O III]λ 4363 is increased by only 1%. Decreasing f_1^{cov} from 0.26 to 0.22, Hβ is recovered by increasing $\tau_m(2)$ and [O II]λ 3727 by decreasing τ_c, with the consequence that P_{in} must decrease, thus T_e increase and O/H decrease. The λ 4363 intensity increases up to the observed value, [Ar IV]λ 4740 and [S IV]λ 10.5μ increase and [O I]λ 6300 decreases.

5.3.2. Models *M3* and *M4*

In Model *M*3, $T2/10^4$ K is enhanced from 4 to 5. Q_{abs}/Q is larger than in *M*2 due to lower luminosity. The larger $T2$ increases the average energy of photons absorbed in the O^{2+} region and the intensity of [O III]λ 4363 is slightly larger. In the selected example, [O III] is again exactly matched as in *M*2*c*, but for more "standard" f_1^{cov} and f_2^{cov} (Col. 6 of Table 2). Line intensity predictions are slightly improved (Col. 7 of Table 4 versus Col. 4 of Table 5).

In Model *M*4, $T2$ is again as in *M*2, while $T1/10^4$ K is enhanced from 8 to 12 and $L1/L2$ is halved. Q_{abs}/Q is close to its allowed maximum due to radiation hardening, which also leads to $\delta_4 \ll 1$ (Col. 7 of Table 2). The large flux just below 4 ryd enhances simultaneously the high and low ionization lines, but the heating of the O^{2+} region is lesser and the large $T1$ (positive curvature of the SED) does not favour a large r([O III]) (Col. 8 of Table 4). From Table 5, variants *M*4*b* (Col. 5) and *M*4*c* (Col. 7) of *M*4 (Col. 6) fail to enhance [O III]λ 4363 up to the observed value. Increasing the source luminosity by 20%, thus decreasing Q_{abs}/Q from 0.43 to 0.36, has no effect on the predicted [O III] after convergence.

6. Discussion

Irrespective of the "technical" demand raised by Q_{abs}/Q in Sect. 5.2, a two-sector model is the minimum complexity of any shell topology (Sect. 4.2). The two degrees of freedom attached to the matter-bounded sector are inescapable.

Model $M4$ (and variants) appears slightly less successful than $M2$ and $M3$ concerning [O III]λ 4363 and the high-ionization lines ([Ar IV]λ 4740, [S IV]λ 10.5μ). $M4$ has a less likely SED and presents the largest P_{out}/P_{in}. The discussion focuses on Models $M2$ and $M3$, with $M2$ the "standard" from which variants are built.

6.1. Spectral energy distribution

Accounting for a Q_{abs}/Q larger than, say, 1/3 turns out to be demanding. Selected models correspond to nearly maximum possible values for each SED. Acceptable Q_{abs}/Q can indeed be obtained, but the latitude on the SED and power of the ionizing source is narrow. The uncertainties in evolutionary synthetic cluster models (Appendix C) and in the evolutionnary status of I Zw 18 NW itself are sufficient to provisionally accept the "empirical" SED corresponding to preferred models $M2$ or $M3$ (Fig. 1) as plausible. The "predicted" typical trend is $L_\nu(h\nu = 1 \rightarrow 4 \text{ ryd}) \propto \exp(-h\nu/\text{ryd})$.

6.2. Ionized gas distribution

The model is most specific in that emission lines partly arise from a low density gas, while the largest N_e is N_e([S II]). A density $\leq$10 cm^{-3} (Table 2) appears very low by current standards of photoionization models for BCDs (Appendix A.1). Nevertheless, the superbubble model of Martin (1996) is consistent with a current $SFR = 0.02\ M_\odot\ \text{yr}^{-1}$ for the whole NW+SE complex. The two best estimates in the compilation by Wu07 are 0.03 and 0.02 $M_\odot$ yr^{-1}. Adopting half the Martin (1996) rate and a wind injection radius of 0.1 kpc (1.5″ at 13 Mpc) for the NW cluster alone, expression (10) in Veilleux et al. (2005) suggests an inner pressure of the coronal gas $P/k \sim 3 \times 10^5$ K cm^{-3}, hence an ambient ISM number density $\sim$12 cm^{-3} in the inner region ($T_e \sim 2.5 \times 10^4$ K; Sect. 5), or else $N_H \sim 12/2.3 = 5$ cm^{-3} for a photoionized gas in pressure balance with the coronal phase which presumably permeats the shell. Although ϵ is unity in models, this phase can fill in the volume corresponding to Sector 3.

6.3. Optical and UV lines

[O III] lines are discussed in Sects. 6.7 and 6.8. C IV and Si III] are accounted for within uncertainties. Other UV lines are elusive (Col. 6 of Table 3).

Computed fluxes for 8 optical lines are within 20% of observation (Table 4), which is satisfactory considering the weakness of some of the lines. The 10−15% discrepancy on the ratio [S III] 6312/9531 does not challenge the model itself, given the various uncertainties. The $\sim$20% underestimation of [S II] should be considered with respect to [S III]. The line λ 9531 is matched, but the far-red flux may be less reliable, and λ 6312 departs from observations about in the same way as [S II], but λ 6312 is a weak line. The exact status of [S II] is undecided.

The N_e-sensitive intensity ratio [Fe III]λ 4986/λ 4658 is somewhat small in $N0$, large in $N1$ and more nearly correct in Mi models. Would [S II] be emitted in a high-N_e gas component as suggested by SS99 and V02, then [Fe III] 4986, roughly co-extensive with [O II], would be undetectable. The weak line [Fe IV] 4906, co-extensive with [O III], confirms the ion distribution of the Mi models and the iron abundance, although the agreement with observation is partly fortuitous. [Fe V] 4227 is overpredicted by a factor $\sim$3, but the observed intensity is very uncertain and could be 2−3 times stronger than the quoted value, as judged from published tracing (TI05). Also, only one computation of collision strengths has ever been done for the optical lines of the difficult [Fe V] ion (Appendix D.3). Finally, the ionic fraction Fe^{4+}/Fe, less than 5%, is subject to ionization balance inaccuracy. The predicted intensity $\sim I(\lambda\,4227\ \text{Å})/4$ of [Fe V] 4071 enhances the computed flux of [S II] 4068 up to the observed value (Tables 3 and 4).

The observed He I line intensities are inconsistent (Table 3), due to stellar lines (Sect. 4.3). [Ar IV] 4711, blended with He I 4713, is therefore useless. The weak [Ar IV] 4740 tends to be overestimated by $\sim$50% in the preferred models. Trial calculations show that, adopting a recombination coefficient 12 times the radiative one (instead of 8 times, Appendix D.3) and dividing Ar/H by 1.13, [Ar III] and [Ar IV] would be matched in $M2$.

6.4. Infrared fine-structure lines

6.4.1. [NeIII] and [SIII]

The reliably observed IR lines with optical counterparts, [Ne III] 15.5μ and [S III] 18.7μ, are very well matched, confirming the scaling adopted for the SPITZER fluxes and the model temperatures. The Mi models, globally hotter, are more successful than the Ni runs. No t^2 in excess of the one of the adopted configuration (Fig. 8d) is required.

The predicted intensity of [S III] 33.5μ is only 40% of the observed value. Since the theoretical ratio of the [S III] IR lines is insensitive to conditions in I Zw 18, looking for alternative models is hopeless. The collision strengths Ω for the [S III] lines may not be of ultimate accuracy, as the results of Tayal & Gupta (1999) and Galavis et al. (1995) differ, but the more recent Ω are likely more accurate. Also, the predicted [S III] 33.5μ is even worse using older data. Since Wu07 cast doubt on the accuracy of the flux calibration at the end of the SPITZER spectrum, it is assumed that the [S III] atomic data are accurate and that the observed fluxes around λ 34μ should be divided by 2.3.

6.4.2. [OIV]

If the drift of flux calibration at λ 34μ (Sect. 6.4.1) smoothly vanishes towards shorter wavelengths, the [O IV] 26μ flux may still be overestimated. Conversely, the SPITZER field of view encompasses I Zw 18 SE, which emits little He II, leading to underestimate [O IV]/Hβ in I Zw 18 NW. Since these effects act in opposite directions, the original [O IV]/Hβ is adopted for I Zw 18 NW.

As shown in Fig. 5, O^{3+} and O^{2+} coexist in the He^{2+} zone. O^{3+}/O^{2+} and therefore [O IV]λ 25.88μ/He IIλ 4686 as well are sensitive to N_e. In $N0$, He II is matched and [O IV] is strongly underpredicted (Table 4). The predicted [O IV] flux improves in the conditions of $N1$ and even by-pass observation in $M1$, whose ionizing flux is however too large (Sect. 5.2). In the standard Model $M2$, the predicted [O IV] exactly matches observation after adding the blended line [Fe V] 25.91μ, whose computed flux is $\sim$2% of [O IV]. Since relevant atomic data are reliable, [O IV] 25.88μ indicates that N_e must be of the order of 10 cm^{-3} in the He II emitting region of the I Zw 18 NW shell. The model density results from general assumptions (photoionization by stars, shell geometry, $\epsilon = 1$, Eq. (1), etc.) and a requirement

to match a few basic line intensities with no reference to high-ionization lines, but He II. The computed [O IV] intensity is a true prediction, especially as the models were essentially worked out prior to IR observations: the spectrum presented by Wu et al. (2006) showed the predicted [O IV] line, finally noted by Wu07.

6.4.3. [S IV]

The predicted [S IV] 10.5μ flux is twice the observed one. The collision strengths obtained by Tayal (2000) and Saraph & Storey (1999) for this line are in good agreement. The average fractional concentration of S^{3+}, ~1/3, is stable in different models because sulfur is mostly distributed among the three ions S^{2+}–S^{4+}. Displacing the ionization balance by changing, e.g., the gas density tends to make either S^{2+} or S^{4+} migrate to S^{3+}. Only in the unsatisfactory run *N*0 is [S IV] accounted for.

Two-sector, constant-pressure "models" allowing $\epsilon < 1$ and using the SED of Model *M*2 were run with the conditions $Q_{abs}/Q > 0.3$ and O/H $< 1.7 \times 10^{-5}$. In these trials, the [O III] 5007 and *r*([S II]) constraints (Table 1) are relaxed and the observed [S IV]/[S III] ratio is exactly matched varying N_e (gas pressure) and ϵ. Despite ample freedom and because of the higher $N_e \sim 25$ cm^{-3}, the computed [O IV] flux is at most 60% of the observed one. Thus, forgetting other difficulties, the suggestion is that the excess [S IV] flux can only be cured at the expense of [O IV]. A broader exploration of the SED (discontinuities) and the gas distribution could be undertaken.

The [S IV] 10.5μ flux published by Wu et al. (2006) was 25% larger than according to Wu07. The new value should be preferred, but this difference is at least indicative of possible uncertainties. The ratio [S IV]/Hβ may also be intrinsically larger in I Zw 18 NW than in I Zw 18 SE.

The theoretical ionization balance of some ions of sulfur (and argon) is subject to uncertainties (Appendix D.3). The observed [S IV]/[S III] ratio can be recovered in *M*2 if the S^{2+} recombination coefficient is multiplied by a factor of 2.3, which is perhaps acceptable (Badnell 2007, private communication): then, both [S III] and [S IV] are matched if S/H is divided by 1.33, with the caveat that the predicted [S II] intensities are divided by 1.3. A combination of observational and theoretical effects just listed could alleviate the "[S IV] problem".

6.5. Low ionization fine-structure lines

Although the error bars of order 10% quoted by Wu07 may not include all sources of uncertainties, both [Ne II] 12.78μ and [Fe II] 25.98μ are detected in high-resolution mode. [Si II] 34.80μ is strong, even though the flux quoted by Wu07 (Table 4) may be too large (Sect. 6.4.1). Usually, most of [Si II] 35μ and [Fe II] 26μ arise from a Photon-Dominated Region (PDR), at the warm H I interface between an ionization front and a molecular cloud (e.g., Kaufman et al. 2006). Schematically in a PDR, the photo-electric heating by UV radiation on dust grains (and other molecular processes) is balanced by fine-structure (and molecular) line emission. The small reddening intrinsic to I Zw 18 (Sect. 3.2) and the "large" gaseous iron content (Sect. 6.7) imply that little dust is available. Molecules and PAHs are not detected in I Zw 18 (Vidal-Madjar et al. 2000; Leroy et al. 2007; Wu07). The classical PDR concept may therefore not apply to I Zw 18, raising the question of the origin of [Si II] 35μ and [Fe II] 26μ, both underpredicted by factors of 5–10 in the models (Table 4).

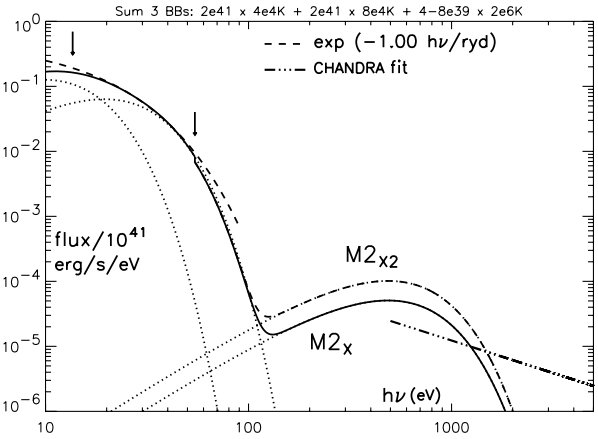

Fig. 6. As in Fig. 1b for variants of *M*2 comprising a soft X-ray emitting black body: Model $M2_X$ (solid line) and $M2_{X2}$ (dash-dotted line). Ordinate unit flux is now 10^{41} erg s^{-1} eV^{-1}. Dash-triple-dotted line: one possible fit to the CHANDRA data for I Zw 18 NW.

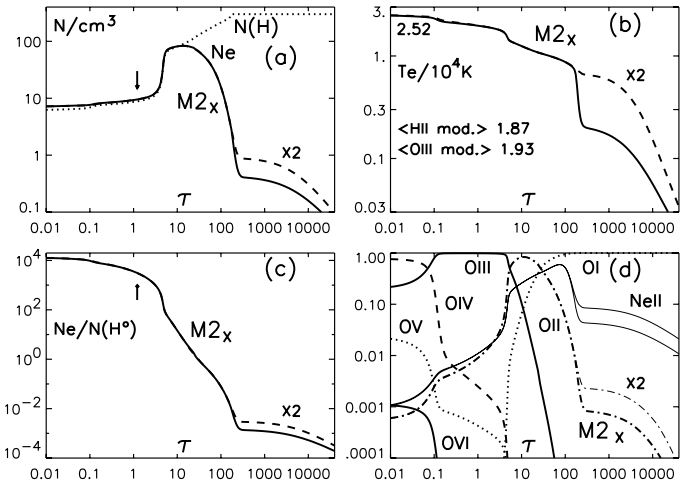

Fig. 7. Model $M2_X$ for I Zw 18 NW. **a)** Electron density N_e (solid line) and total hydrogen density N(H) (dotted line) versus optical depth τ at 1 ryd: N(H) levels out at 300 cm^{-3}. **b)** Electron temperature $T_e/10^4$ K: the maximum value and average values weighted by $N_e \times N(H^+)$ and by $N_e \times N(O^{2+})$ are noted for the full 2-sector model (⟨mod.⟩). **c)** Ratio of N_e to atomic hydrogen density $N(H^0)$. In panels **a)**–**c)**, the dashed lines correspond to $M2_{X2}$. **d)** Local fractional concentrations of O^0 (dotted line), O^+ (dot-dashed line), O^{2+} (solid line), O^{3+} (dashed line), O^{4+} (dotted line again) and O^{5+} (solid line again): the thinner dash-dotted line ($\tau > 200$) corresponds to O^+ in $M2_{X2}$ and the thinner solid line (split into $M2_X$ and $M2_{X2}$ for $\tau > 200$) to Ne^+.

A way to produce a "pseudo-PDR" is X-ray heating. Two new variants of *M*2 are considered, in which a hot black body representing a soft X-ray emission from I Zw 18 NW is added to the original SED. The adopted temperature is $T_X = 2 \times 10^6$ K and the luminosity $L_X = 4$ and 8×10^{39} erg s^{-1} for variants $M2_X$ and $M2_{X2}$ respectively (Fig. 6). The actual X-ray luminosity of I Zw 18, ~1.6×10^{39} erg s^{-1} in the 0.5–10 kev range of CHANDRA mainly arises from the centre of I Zw 18 NW and is consistent with a power law of slope −1 (Thuan et al. 2004), drawn in Fig. 6. The SED for $M2_X$ is a relatively high, yet plausible extrapolation of the CHANDRA data. $M2_{X2}$ is considered for comparison. N_H, still governed by Eq. (1), levels out at 300 cm^{-3}.

The run of physical conditions with τ is shown in Fig. 7 for $M2_X$. While $\langle T_e \rangle$ is increased by only ~100 K in the H II region,

Table 6. Fine-structure line intensities[a] and X-rays.

Line[b]	Obs.	$M2$		$M2_X$		$M2_{X2}$	
H I colls.[c]	–	no	yes	no	yes	no	yes
[C II] 158.	–	2.1	2.1	124	119	224	204
[O I] 63.2	–	4.7	4.6	274	210	624	450
[Ne II]12.8	9	1.9	3.6	1.9	5.5	2.0	16
[Si II] 34.8	157[d]	21	22	37	80	55	190
[Ar II] 7.0	–	1.2	1.3	1.4	2.2	2.2	7.9
[Fe II] 26.0	34	3.4	4.8	5.8	38	9.3	108
[Fe II] 35.3	–	0.8	1.4	1.1	9.5	1.7	33

[a] In units Hβ = 1000. [b] Wavelengths in μm. [c] Inelastic collisions of [Si II], [Fe II], [Ne II] and [Ar II] with H I omitted ("no") or included ("yes"). [d] The re-calibrated [Si II] flux is 68 after Sect. 6.4.2.

a warm low-ionization layer develops beyond the ionization front. The computation is stopped at T_e = 100 K ($\tau \sim 7 \times 10^4$, compared to 250 in $M2$). In $M2_{X2}$ (dashed lines in Figs. 7a–c), the new layer is hotter and more ionized (final $\tau \sim 1.2 \times 10^5$). The geometrical thickness of the H I layer is 21% and 35% of the H II shell in $M2_X$ and $M2_{X2}$ respectively. In the H I zone, O^+/O does not exceed $\sim 10^{-3}$, in marked contrast with Ne^+/Ne, overplotted as a thin solid line in Fig. 7d. Lines [Ne II] 12.8μ and [Ar II] 7.0μ are usually discarded in PDR models on the basis that the ionization limits of Ne^0 and Ar^0 exceed 1 ryd. Here, owing to the scarcity of free electrons and the lack of charge exchange with H^0, photoionization by soft X-rays can keep 1–10% of these elements ionized.

In H I regions, cooling is due to inelastic collisions with H^0. Reliable collisional rates exist for the main coolents [C II] 157μ (Barinovs et al. 2005) and [O I] 63μ (Abrahamsson et al. 2007; several processes need be considered for [O I]: see Chambaud et al. 1985; Péquignot 1990) and for [Si II] 35μ (Barinovs et al. 2005), but not for, e.g., [Fe II] 26μ. Following Kaufman et al. (2006), it is assumed that the cross-section for $H^0 + Si^+$ also applies to fine-structure transitions of other singly ionized species. Concerning [Fe II] (ground state $^6D_{9/2}$), collisions to $^6D_{7/2}$ follow the above rule, but cross-sections for transitions to the next ^6D_J are taken as 2/3, 2/4, etc. of the first one.

Low-ionization IR lines, including dominant coolents and other unobserved lines, are considered in Table 6. Line identifications and observed intensities appear in Cols. 1 and 2. The results of two computations are provided for $M2$ (Cols. 3, 4), $M2_X$ (Cols. 5, 6) and $M2_{X2}$ (Cols. 7, 8). In the first one, the excitations of [Si II], [Fe II], [Ne II], and [Ar II] (but not [O I] and [C II]) by collisions with H I are inhibited. In the second one, they are included according to the above prescription. Comparing different odd columns ("no") of Table 6, the rise of line intensities as the H I zone develops shows that the excitation of, e.g., [Si II] by free electrons is still active. [Ne II] is stable, due to the scarcity of Ne^+ (Fig. 7d) relative to Si^+. Comparing now odd columns to even columns, it is seen that H I collisions, ineffective in the "normal" H II region model $M2$ (except, quite interestingly, for [Ne II]), strongly enhance the excitation rates. After subtracting emission from the H II region ($M2$), H I collisions contribute 75–80% of the excitation (virtually 100% in the case of [Ne II]).

Concerning [Si II] 35μ, the atomic data are not controversial and the re-calibrated flux of 68 is reasonably well defined (Sect. 6.4.2). Then $M2_{X2}$ (Col. 8 of Table 6) is excluded, while $M2_X$ (Col. 6) or an even weaker soft X-ray source (closer to the CHANDRA extrapolation) can account for [Si II]. Although the remarkably coherent predictions for [Si II] 35μ and [Fe II] 26μ are partly fortuitous, they are consistent with (1) the [Fe II] collision strength being correctly guessed, (2) Fe/Si the same in the ionized and neutral gas, and (3) the excitation by soft X-ray heating is viable. Concerning [Ne II] 12.8μ, the discrepancy with observation (factor 0.6) may not be significant, as the line is weak and its detection in the low-resolution mode is not taken as certain by Wu07. The collision strength may be too small.

Summarizing, a plausible extrapolation to soft X-rays of the CHANDRA flux can provide an explanation for the relatively high intensity of [Si II] 35μ and other fine-structure lines in I Zw 18. This is considerable support to the general picture of photoionization as the overwhelmingly dominant cause of heating of the H II region, since heating by conversion of mechanical energy appears unnecessary even in regions protected from ionization and heating by star radiation. Full confirmation should await reliable collisional excitation rates by H I for fine-structure lines of all singly ionized species. The soft X-rays from I Zw 18 NW have little effect on the H II region: both [O I] 6300 and [O IV] 25.9μ are increased by 3% and [Fe VI] by 30%. The 1.7% enhancement of [O III] 4363 is of interest (Sect. 6.8).

6.6. Stability of results

The relative stability of the predicted line intensities is a consequence of the set of constraints (Table 1). Allowing for a range of values, a broader variety of results could be obtained. Are the conclusions dependent on input data?

The only basic line showing substantial variability in different spectroscopic studies is [O II] 3727. This line is sometimes found to be stronger than the adopted value (VI98; TI05). In a new variant $M2v$ of Model $M2$, the observed [O II] intensity is assumed to be 20% larger than in Tables 3 and 4 and the covering factors are left unchanged. The inevitable 18% increase of the already too strong line [O II] 7320+30 is not very significant, considering that the λ 7325 flux is very uncertain and may not correspond to a slit position with stronger λ 3727. Due to the larger fractional abundance of O^+, O/H is increased by 5%. The greater weight of low-ionization layers induces a 3% increase of Ne/H and a 13% decrease of N/H and Fe/H, as the [N II] and [Fe III] intensities were left unchanged. Both [Ar IV] and [S IV] decrease by a few %, whilst [O IV] increases by 6% and both [S II] and [O I] increase by ~11%. Ar/H and the [S III] lines increase by only 1% and [O III]λ 4363 is unchanged.

In a more extreme example, $M2cv_X$, with an assumed [O II] intensity of 322 instead of 238 (factor 1.35), the fs as in $M2c$ and the SED as in $M2_X$ (re-converged τ_c = 2.5 and P_{in}/P_{out} = 9), [O III] is exactly matched again, [O I] is +2% off, [O IV] +6%, [S IV] +87% and [S II] only −8%.

Thus, changes are moderate and alleviate difficulties noted in Sects. 6.3 and 6.4, e.g., the weakness of the [S II] doublet. The computed r[O III] is robust.

6.7. Elemental abundances

To first order, O/H reflects $\langle T_e(O^{2+})\rangle$, related to r([O III]), i.e., the predicted [O III]λ 4363 intensity. Models $M3$ and $M2c$ both almost exactly fit λ 4363 and share the same O/H = 1.62×10^{-5}, which is the best estimate, provided that (1) oxygen lines were given optimal observed intensities, (2) these models faithfully represent the H II region, and (3) collision strengths are accurate.

Concerning line intensities, [O III] 5007 is quite stable in different spectra of I Zw 18 NW and the reasonably large, yet representative, ratio r([O III]) (Sect. 3.3) is taken for granted, since our objective is deciding whether this specific ratio can be explained

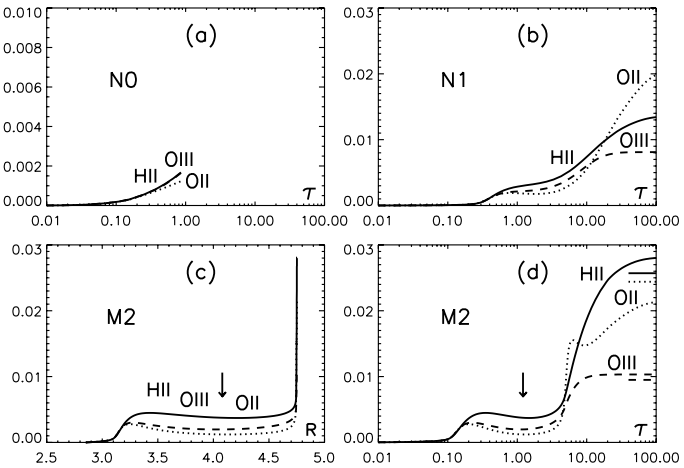

Fig. 8. Cumulative mean squared relative temperature fluctuations t^2 (Peimbert 1967) weighted by $N_e \times N(H^+)$ (solid line), $N_e \times N(O^+)$ (dotted line) and $N_e \times N(O^{2+})$ (dashed line) versus τ in I Zw 18 NW models: **a)** $N0$, **b)** $N1$, **d)** $M2$; and versus R: **c)** $M2$. Note the expanded vertical scale in panel **a)**. The short horizontal bars to the right of panel **d)** correspond to the means over the full model. Vertical arrows as in Fig. 3.

assuming photoionization by stars. In model $M2cv_X$ (Sect. 6.6), which also fits the [O III] lines, [O II] 3727 was assumed to be enhanced by 35%, leading to O/H = 1.74×10^{-5}.

Concerning models, the difference between the T_e directly derived from r([O III]), T_e([O III]) = 19 850 K, and the $N_e \times N(O^{2+})$ weighted average, $\langle T_e(O^{2+})\rangle$ = 19 650 K, corresponds to a formal t^2([O III]) = 0.012, similar to the computed $t^2(O^{2+})$ = 0.010. This difference makes only a 1% difference for O^{2+}/H^+ and an empirical estimate neglecting t^2 should nearly coincide with model results for this ion. A major feature of the T_e profile is that the difference $\langle T_e(O^{2+})\rangle - \langle T_e(O^+)\rangle$, which was only 300 K in $N0$ and 3200 K in $N1$, is 6600 K in the best models. The models are essential in providing a T_e to derive O^+/H^+ from [O II] 3727, as T_e([O II]) is poorly determined from the uncertain [O II] 7325 and t^2([O II]) is inaccessible.

A "canonical" O/H for I Zw 18 NW is 1.46×10^{-5} (SK93, ICF99), 11% less than the present 1.62×10^{-5}, out of which 4% are due to collisional excitation of Hβ and the remaining 7% could be a non-trivial consequence of the relatively large t^2 obtained for some ions in the present models (Table 2; Fig. 8), although differences in collision strengths may also intervene at the 2% level (Appendix D.2).

The silicon and sulfur abundances were not fine-tuned in models. The computed Si III] flux loosely suggests dividing the assumed Si/H by 1.25. Concerning S/H, [S II] is underestimated, [S III] globally underestimated and [S IV] overestimated. Correcting the ionization balance [S IV]/[S III], S/H should be divided by 1.3 in the best models (Sect. 6.4.3), but [S II] is then underestimated. Since a combination of effects may explain the overestimation of [S IV], the model S/H is tentatively divided by 1.15. Similarly, [Ar IV]/[Ar III] is best accounted for if Ar/H is divided by 1.13 (Sect. 6.3), but the [Ar IV] line is weak. The adopted correction factor is 1.06. Thus, S/Ar in I Zw 18 is within 10% of the solar value, in agreement with the conclusion of Stevenson et al. (1993). The iron abundance relies on the [Fe III] lines, since [Fe II] 26μ does not arise from the H II region, while the [Fe IV] and [Fe V] intensities are uncertain. The [Fe III] intensities are from a spectrum in which [O II] 3727 is stronger than average (TI05). In variant $M2cv_X$ (Sect. 6.6), where the intensity of [O II] is multiplied by 1.35, both the predicted [Fe IV] 4906 and Fe/H are divided by 1.4. This lower Fe/H is adopted.

Table 7. Abundances in I Zw 18 NW compared to solar and Galactic halo stars.

El.	M^a	X/O M	X/O IT^b	[X/H] M	[X/Fe] M	[X/Fe] H^c
C	6.55	−0.66	−0.77	−1.84	−0.02	−0.05 ± 0.15
N	5.60	−1.61	−1.56	−2.18	−0.36	−0.40 ± 0.30
O	7.21	–	–	−1.45	0.37	0.52 ± 0.15
Ne	6.39	−0.82	−0.80	−1.45	0.37	–
Si	5.89	−1.32	−1.46	−1.62	0.20	0.21 ± 0.08
S	5.57	−1.64	−1.55	−1.57	0.25	0.21 ± 0.07
Ar	4.97	−2.24	−2.16	−1.55	0.27	–
Fe	5.63	−1.58	−1.45	−1.82	–	–

[a] 12 + log (X/H) by number in present model M.
[b] Empirical abundance: Izotov & Thuan (1998, 1999) with 12 + log (O/H) = 7.16; Fe: Thuan & Izotov (2005).
[c] Halo stars [Fe/H] ∼ −1.8: Fabbian et al. (2006); García Pérez et al. (2006); Nissen et al. (2007); Carbon et al. (1987).

Solar abundances are tabulated by Asplund et al. (2005, AGS05). The compilation by Lodders (2003) is in agreement with AGS05 (+0.03 dex for all O−S elements of interest here and +0.02 dex for Fe relative to H), except for Ar/H (+0.37 dex). The larger argon abundance is convincingly advocated by Lodders (2003). Ar/O is adopted from this reference. Then Ar/H coincides with the value listed by Anders & Grevesse (1989). The shift of O/H from Anders & Grevesse (1989) to AGS05 is −0.27 dex, out of which −0.07 dex corresponds to the change from proto-solar to solar abundances. Shifts for X/Fe are ∼−0.20 dex for N, O, Ne, −0.11 dex for C, −0.07 dex for S and ∼0.0 for other elements of interest.

In Table 7, the present model abundances by number 12+log(X/H) for I Zw 18 NW ("M") are provided in Col. 2. The abundances X/O relative to oxygen from models (Col. 3, "M") are compared to empirical values obtained by IT99 (Col. 4, "IT"). The brackets [X/Y] = log (X/Y) − log $(X/Y)_\odot$ from models are given in Cols. 5 and 6 (Y ≡ H and Fe). [X/Fe] is provided for Galactic Halo stars with [Fe/H] ∼ −1.8 (Col. 7, "H"). Despite considerable efforts to include 3D and non-LTE effects in the study of line formation in cool stars, astrophysical descriptions and atomic data may still entail uncertainties in stellar abundances (e.g., Fabbian et al. 2006), particularly for nitrogen. A population of N-rich stars is identified (e.g., Carbon et al. 1987).

Comparing Cols. 3 and 4, the model and empirical X/O agree to about 0.1 dex. The present C/O is close to the one obtained by Garnett et al. (1997), who claim that C/O is anomalously large in I Zw 18. IT99 argue that the subregion of I Zw 18 NW observed with the HST is especially hot according to spatially resolved MMT data and that C/O is therefore small. Nonetheless, IT99 also derive an exceedingly low O/H at the same position "because of the higher T_e", which poses a problem of logic since there is a priori no link of causality between T_e and O/H within I Zw 18. The [C/O] = −0.39 resulting from the present model is indeed marginally incompatible with the up-to-date [C/O] = −0.57 ± 0.15 corresponding to Galactic Halo stars with [O/H] = −1.45 (Fabbian et al. 2006). This "large" [C/O] is analysed by Garnett et al. (1997) in terms of carbon excess, suggesting that an old stellar population managed to produce this element, then challenging the view that I Zw 18 is genuinely young (e.g., IT04), a view also challenged by Aloisi et al. (2007). From models, [C/Fe] appears to be identical in I Zw 18 and halo stars of similar metallicity (Cols. 6 and 7). The relatively large [C/O] in

I Zw 18 is due to a relatively small [O/Fe]. This is indirectly confirmed by the agreement between I Zw 18 and halo stars for all elements beyond neon (argon should follow lighter α-elements). The [X/O]s ($\equiv$[X/H] + 1.45) are the usual basis to discuss elemental abundances in BCDs and nebulae. Exceptionally, in I Zw 18, the abundances of iron and heavy α-elements agree, allowing us to consider the oxygen abundance with respect to metallicity, instead of defining metallicity by means of oxygen itself. Any iron locked into dust grains would further decrease [O/Fe] in I Zw 18. Apparently, for sufficiently low metallicity of the ISM and/or sufficient youth of the host galaxy, iron does not find paths to efficiently condense into dust. Alternatively, dust grains may be destroyed by shocks.

6.8. Overall evaluation of models

Line intensities are generally well accounted for, although [S IV]λ 10.5μ is overpredicted by 90−100% (Sect. 6.4.3).

The freedom left in the parameters describing the SED and the shell acts at the few % level upon the [O III]λ 4363 predicted intensity. Thus, the calculated [O III]λ 4363 shifts from 96.0% of the observed intensity in $M2$ ($T2 = 4 \times 10^4$ K, $f_i^{\rm cov} = 0.26$, 0.30) to 99.6% in $M2c$ ($f_i^{\rm cov} = 0.22$, 0.60) and 99.8% in M3 ($T2 = 5 \times 10^4$ K, $f_i^{\rm cov} = 0.23$, 0.50). Adding less than 1% luminosity as soft X-rays (e.g., $M2_{\rm X}$, compared to $M2$, Sect. 6.5) results in +1.7% for [O III]λ 4363. Also, increasing He/H from 0.080 to the possibly more realistic value 0.084 (Peimbert et al. 2007), [O III]λ 4363 is enhanced by a further +0.6%. Since both the X-ray and He/H corrections are plausible, it is relatively easy to reach 100−102% of the observed [O III]λ 4363 intensity in the assumed configurations.

However, models tell us that r([O III]) can hardly be larger than the observed value. It may prove necessary to consider alternative gas distributions, e.g., if the [S IV] misfit is confirmed by more accurate observational and theoretical data. Assuming higher densities in the diffuse medium (Sect. 6.4.3) and/or considering thick filaments closer to the source tend to penalize [O III]λ 4363.

Uncertainties on [O III] collision strengths Ω need to be considered (Appendix D.2). Using Ωs by Lennon & Burke (1994, LB94) instead of Aggarwal (1993, Ag93), the computed λ 4363 would be 2.1% smaller and more difficult to explain. On the other hand, using $\Omega(^3{\rm P} - {}^1{\rm D})$ from Ag93 and $\Omega(^3{\rm P} - {}^1{\rm S})$ from LB94 would enhance all computed λ 4363 intensities by 2.1%. Concerning transition $^3{\rm P} - {}^1{\rm S}$ which controls λ 4363, both Ag93 and LB94 find a 5−6% increase of Ω from 2×10^4 K to 3×10^4 K, due to resonances. If for some reason the energy of these resonances would be shifted down, there would be room for a few % increase of Ω at 2×10^4 K compared to the current value, then introducing more flexibility in the present model of I Zw 18.

Thus, the hypothesis of pure photoionization by stars in the form explored here is strong, but the models approach a limit. This is satisfactory, considering that I Zw 18 is an extreme object among BCDs, but sufficient flexibility in choosing solutions is worthwhile. An analysis of how the computed r([O III]) can be influenced shows that, in the case of I Zw 18, possible variations of "astrophysical" origin are of the same order as the uncertainties affecting the Ωs. Since the set of computed r([O III]) tends to be reduced by 2−3% relative to observations, it is legitimate to question the Ωs. The recent re-evaluation of the distance to I Zw 18 by Aloisi et al. (2007) may offer an "astrophysical alternative": multiplying D, $R_{\rm i}$ and $R_{\rm f}$ by $2^{1/2}$ and the luminosty by 2, the relative volume increase leads to smaller $P_{\rm in}$ and $\tau_{\rm c}$, and, after reconvergence, [O III]λ 4363 is enhanced by +2.4%. Nonetheless, [S IV] 10.5μ is enhanced too (+5%).

7. Concluding remarks

Due to its small heavy element content, I Zw 18 stands at the high-$T_{\rm e}$ boundary of photoionized nebulae. Where ionization and temperature are sufficiently high, the cooling is little dependent on conditions, except through the relative concentration of H^0, controlled by density. Therefore, from a photoionization model standpoint, $T_{\rm e}$ is then a density indicator, in the same way that it is an O/H indicator in the usual H II regions. It is for not having recognized the implications of this new logic that low-metallicity BCD models failed.

In a photoionization model study of I Zw 18 NW, SS99 employed a filling-factor description and concluded that $T_{\rm e}$([O III]) was fundamentally unaccountable for. This description of the ionized gas owes its popularity to its simplicity and to its apparent success for usual H II regions. This success is no warranty for exactness, however, since it is based on the strong dependence of gas cooling on abundances and the filling-factor concept fails when applied to low-Z GEHIIRs. This conclusion of SS99 and other authors should be paralleled with the "t^2 problem" (Esteban et al. 2002; Peimbert et al. 2004), which calls into question the assumption of photoionization by stars as the overwhelmingly dominant source of heat in gaseous nebulae since the presence of $T_{\rm e}$ fluctuations *supposedly larger* than those reachable under this assumption implies additional heating.

A conclusion of the present study is that the gas distribution is no less critical than the radiation source in determining the line spectrum of H II regions. Assuming pure photoionization by stars, the implication of the large $T_{\rm e}$([O III]) of I Zw 18 NW is that the mean density of the [O III] emitting region is much less than $N_{\rm e}$([S II]), a low $N_{\rm e}$ confirmed by line ratios [O IV]λ 25.9μ/He IIλ 4686 and [Fe III]λ 4986/[Fe III]λ 4658. I Zw 18 NW models comprising a plausible SED and respecting geometrical constraints can closely match almost all observed lines from UV to IR, including the crucial [O III]λ 4363 ([S IV]λ 10.5μ is a factor of 2 off, however). Thus, extra heating by, e.g., dissipation of mechanical energy in the photoionized gas of low-metallicity BCD galaxies like I Zw 18 is not required to solve the "$T_{\rm e}$([O III]) problem". Moreover, since low-ionization fine-structure lines observed in I Zw 18 can be explained by soft X-rays, (hydrodynamical) heating is not required either in warm H I regions protected from heating by star radiation.

The solutions found here are marginally consistent with observed r([O III]). Given the claimed accuracy in the different fields of physics and astrophysics involved, postulating a mechanical source of heating is premature, whereas a 2−3% upward correction to the collision strength for transition $O^{2+}(^3{\rm P} - {}^1{\rm S})$ at $T_{\rm e} \sim 2 \times 10^4$ K is an alternative worth exploring by atomic physics. Another possibility is a substantial increase of the distance to I Zw 18. From accurate spectroscopy and the peculiar conditions in I Zw 18, astrophysical developments are at stake in the 5% uncertainty attached to [O III] collision strengths.

If photoionized nebulae are shaped by shocks and other hydrodynamic effects, this does not imply that the emission-line intensities are detectably influenced by the thermal energy deposited by these processes. Unravelling this extra thermal energy by means of spectroscopic diagnostics and models is an exciting prospect whose success depends on a recognition of all resources of the photoionization paradigm. Adopting the view

that photoionization by radiation from young hot stars, including WR stars, is the only excitation source of nebular spectra in BCD galaxies, yet without undue simplifications, may help progress in the studies of stellar evolution, stellar atmosphere structure, stellar supercluster properties, giant H II region structure and finally possible sources of extra thermal energy.

References

Abrahamsson, E., Krems, R. V., & Dalgarno, A. 2007, ApJ, 654, 1171
Aggarwal, K. M. 1983, ApJS, 52, 387
Aggarwal, K. M. 1993, ApJS, 85, 197 (Ag93)
Aggarwal, K. M., & Keenan, F. P. 1999, ApJS, 123, 311
Aloisi, A., Clementini, G., Tosi, M., Annibali, F., et al. 2007, ApJ, 667, L151
Anders, E., & Grevesse, N. 1989, Geochim. Cosmochim. Acta, 53, 197
Anderson, H., Ballance, C. P., Badnell, N. R., & Summers, H. P. 2000, J. Phys. B, 33, 1255 (+ Erratum 2002, J. Phys. B, 35, 1613)
Asplund, M., Grevesse, N., & Sauval, A. J. 2005, Cosmic Abundances as Records of Stellar Evolution and Nucleosynthesis, ed. T. G. Barnes, & F. N. Bash, ASP Conf., 336, 25
Badnell, N. R. 1991, ApJ, 379, 356
Badnell, N. R. 2006, ApJS, 167, 334
Bakes, E. L. O., & Tielens, A. G. G. M. 1994, ApJ, 427, 822
Barinovs, G., van Hemert, M. C., Krems, R., et al. 2005, ApJ, 620, 537
Barragán, P., Errea, L. F., Méndez, L., et al. 2006, ApJ, 636, 544
Brown, T. M., Heap, S. R., Hubeny, I., Lanz, T., & Lindler, D. 2002, ApJ, 579L
Burke, V. M., Lennon, D. J., & Seaton, M. J. 1989, MNRAS, 236, 353
Callaway, J. 1994, ADNDT, 57, 9
Campbell, A. 1990, ApJ, 362, 100
Cannon, J. M., Skillman, E. D., Garnett, D. R., & Dufour, R. J. 2002, ApJ, 565, 931 (CSGD02)
Carbon, D. F., Barbuy, B., Kraft, R. P., et al. 1987, PASP, 99, 335
Cerviño, M., & Luridiana, V. 2006, A&A, 451, 475
Cerviño, M., Mas-Hesse, J. M., & Kunth, D. 2002, A&A, 392, 19
Cerviño, M., Luridiana, V., Pérez, E., et al. 2003, A&A, 407, 177
Chambaud, G., Levy, B., Millie, P., et al. 1980, J. Phys. B, 13, 4205
Crowther, P. A. 2007, ARA&A, 45, 177
Crowther, P. A., & Hadfield, L. J. 2006, A&A, 449, 711
Davidson, K., & Kinman, T. D. 1985, ApJS, 58, 321
de Mello, D. F., Schaerer, D., Heldmann, J., & Leitherer, C. 1998, ApJ, 507, 199
Dufour, R. J., & Hester, J. J. 1990, ApJ, 350, 149
Dufour, R. J., Garnett, D. R., & Shields, G. A. 1988, ApJ, 332, 752
Eissner, W., & Seaton, M. J. 1974, J. Phys. B, 7, 2533
Eissner, W., Martins, P. de A. P., Nussbaumer, H., et al. 1969, MNRAS, 146, 63
Esteban, C., Peimbert, M., Torres-Peimbert, S., et al. 2002, ApJ, 581, 241
Fabbian, D., Asplund, M., Carlsson, M., & Kiselman, D. 2006, A&A, 458, 899
Galavis, M. E., Mendoza, C., & Zeippen, C. J. 1995, A&AS, 111, 347
Galavis, M. E., Mendoza, C., & Zeippen, C. J. 1997, A&AS, 123, 159 (GMZ97)
García Pérez, A. E., Asplund, M., Primas, F., et al. 2006, A&A, 451, 621
García-Vargas, M. L., González-Delgado, R. M., Pérez, E., et al. 1997, ApJ, 478, 112
Garnett, D. R., Skillman, E. D., Dufour, R. J., et al. 1997, ApJ, 481, 174
Giammanco, C., Beckman, J. E., Zurita, A., & Relaño, M. 2004, A&A, 424, 877
González Delgado, R. M., & Pérez, E. 2000, MNRAS, 317, 64
González Delgado, R. M., García-Vargas, M. L., Goldader, J., Leitherer, C., & Pasquali, A. 1999, ApJ, 513, 707
Gräfener, G., & Hamann, W.-R. 2005, A&A, 432, 633
Guseva, N. G., Izotov, Y. I., & Thuan, T. X. 2000, ApJ, 531, 776
Guseva, N. G., Izotov, Y. I., & Thuan, T. X. 2006, ApJ, 644, 890
Henney, W. J., & O'Dell, C. R. 1999, AJ, 118, 2350
Hirashita, H., & Hunt, L. K. 2006, A&A, 460, 67
Hunt, L. K., Dyer, K. K., & Thuan, T. X. 2005, A&A, 436, 837
Hunter, D. A., & Thronson, H. A., Jr. 1995, ApJ, 452, 238
Izotov, Y. I., & Thuan, T. X. 1998, ApJ, 497, 227
Izotov, Y. I., & Thuan, T. X. 1999, ApJ, 511, 639 (IT99)
Izotov, Y. I., & Thuan, T. X. 2004, ApJ, 616, 768 (IT04)
Izotov, Y. I., Foltz, C. B., Green, R. F., et al. 1997a, ApJ, 487, L37
Izotov, Y. I., Thuan, T. X., & Lipovetsky, V. A. 1997b, ApJS, 108, 1
Izotov, Y. I., Chaffee, F. H., Foltz, C. B., et al. 1999, ApJ, 527, 757 (ICF99)
Izotov, Y. I., Chaffee, F. H., Foltz, C. B., et al. 2001a, ApJ, 560, 222
Izotov, Y. I., Chaffee, F. H., & Schaerer, D. 2001b, A&A, 378, L45
Izotov, Y. I., Stasińska, G., Meynet, G., et al. 2006a, A&A, 448, 955
Izotov, Y. I., Schaerer, D., Blecha, A., et al. 2006b, A&A, 459, 71
Jamet, L., Stasińska, G., Pérez, E., et al. 2005, A&A, 444, 723 (JS05)
Kaufman, M. J., Wolfire, M. G., & Hollenbach, D. J. 2006, ApJ, 644, 283
Kunth, D., & Östlin, G. 2000, A&AR, 10, 1
Legrand, F., Kunth, D., Roy, J.-R., et al. 1997, A&A, 326, L17
Leitherer, C. 2006, ASP Conf., Mass loss from stars and the evolution of stellar clusters, in press [arXiv:astro-ph/0608698]
Leitherer, C., Schaerer, D., Goldader, J. D., et al. 1999, ApJS, 123, 3
Lennon, D. J., & Burke, V. M. 1994, A&AS, 103, 273 (LB94)
Leroy, A., Cannon, J., Walter, F., et al. 2007, ApJ, 663, 990
Lodders, K. 2003, ApJ, 591, 1220
Luridiana, V., & Peimbert, M. 2001, ApJ, 553, 633 (LP01)
Luridiana, V., Peimbert, M., & Leitherer, C. 1999, ApJ, 527, 110 (LPL99)
Luridiana, V., Cerviño, M., & Binette, L. 2001, A&A, 379, 1017
Luridiana, V., Peimbert, A., Peimbert, M., et al. 2003, ApJ, 592, 846 (LPPC03)
Maciejewski, W., Mathis, J. S., & Edgar, R. J. 1996, ApJ, 462, 347
Maeder, A., Meynet, G., & Hirschi, R. 2005, The fate of the most massive stars, ed. R. M. Humphreys, & K. Z. Stanek, ASP Conf., 332, 3
Martin, C. L. 1996, ApJ, 465, 680
Martin, C. L. 1997, ApJ, 491, 561
Mendoza, C. 1983, Planetary Nebulae, ed. D. Flower (Reidel), IAU Symp., 103, 143
Meynet, G., & Maeder, A. 2005, A&A, 429, 581
Nahar, S. N. 2000, ApJS, 126, 537
Nissen, P. E., Akerman, C., Asplund, M., et al. 2007, A&A, 469, 319
Oey, M. S., Dopita, M. A., Shields, J. C., & Smith, R. C. 2000, ApJS, 128, 511
Östlin, G. 2000, ApJ, 535, L99
Papaderos, P., Izotov, Y. I., Thuan, T. X., et al. 2002, A&A, 393, 461
Peimbert, M. 1967, ApJ, 150, 825
Peimbert, M. 1995, in The analysis of emission lines, ed. R. Williams, & M. Livio (Cambridge Univ. Press), 165
Peimbert, M., Peimbert, A., Ruiz, M. T., & Esteban, C. 2004, ApJS, 150, 431
Peimbert, M., Luridiana, V., & Peimbert, A. 2007, ApJ, 666, 636
Péquignot, D. 1990, A&A, 231, 499
Péquignot, D., & Tsamis, Y. G. 2005, A&A, 430, 187
Péquignot, D., Ferland, G. J., Netzer, H., et al. 2001, Spectroscopic Challenges of Photoionized Plasmas, ed. G. J. Ferland, & D. W. Savin, ASP Conf., 247, 533
Pradhan, A. K., Montenegro, M., Nahar, S. N., et al. 2006, MNRAS, 366, L6
Przybilla, N., & Butler, K. 2004, ApJ, 610, L61
Relaño, M., Peimbert, M., & Beckman, J. 2002, ApJ, 564, 704
Saraph, H. E., & Storey, P. J. 1999, A&AS, 134, 369
Saraph, H. E., Seaton, M. J., & Shemming, J. 1969, Phil. Tr. R. Soc., A264, 77
Sargent, W. L. W., & Searle, L. 1970, ApJ, 162, L155
Schlegel, D. J., Finkbeiner, D. P., & Davis, M. 1998, ApJ, 500, 525
Seaton, M. J. 1958, Rev. Mod. Phys., 30, 979
Skillman, E. D., & Kennicutt, R. C., Jr. 1993, ApJ, 411, 655 (SK93)
Stasińska, G., & Izotov, Y. 2003, A&A, 397, 71 (SI03)
Stasińska, G., & Leitherer, C. 1996, ApJS, 107, 661
Stasińska, G., & Schaerer, D. 1999, A&A, 351, 72 (SS99)
Stasińska, G., Schaerer, D., & Leitherer, C. 2001, A&A, 370, 1
Stevens, I. R., & Strickland, D. K. 1998, MNRAS, 301, 215
Stevenson, C. C., McCall, M. L., & Welch, D. L. 1993, ApJ, 408, 460
Strickland, D. K., & Stevens, I. R. 1999, MNRAS, 306, 43
Tayal, S. S. 2000, ApJ, 530, 1091
Tayal, S. S. 2006, ApJS, 166, 634
Tayal, S. S. 2006b, J. Phys. B, 39, 4393
Tayal, S. S., & Gupta, G. P. 1999, ApJ, 526, 544
Tenorio-Tagle, G. 1996, AJ, 111, 1641
Tenorio-Tagle, G., Muñoz-Tuñón, C., Pérez, E., et al. 2006, ApJ, 643, 186
Thompson, R. I., Sauvage, M., Kennicutt, R. C., Jr., et al. 2006, ApJ, 638, 176
Thuan, T. X., & Izotov, Y. I. 2005, ApJS, 161, 240 (TI05)
Thuan, T. X., Bauer, F. E., Papaderos, P., & Izotov, Y. I. 2004, ApJ, 606, 213
Tsamis, Y. G., & Péquignot, D. 2005, MNRAS, 364, 687
van Zee, L., Westpfahl, D., Haynes, M. P., & Salzer, J. J. 1998, ApJ, 115, 1000
Veilleux, S., Cecil, G., & Bland-Hawthorn, J. 2005, ARA&A, 43, 769
Vidal-Madjar, A., Kunth, D., Lecavelier des Etangs, A., et al. 2000, ApJ, 538, 77
Viegas, S. M. 2002, RMxA&A (Ser. de Conf.), 12, 219 (V02)
Vílchez, J. M., & Iglesias-Páramo, J. 1998, ApJ, 508, 248 (VI98)
Vink, J. S., & de Koter, A. 2005, A&A, 442, 587
Weise, W. L., Fuhr, J. R., & Deters, T. M. 1996, J. Phys. Chem. Ref. Data, Monograph, 7
Wöste, G., Wunner, G., Noble, C. J., et al. 2002, J. Phys. B, 35, 4847
Wu, Y., Charmandaris, V., Hao, L., et al. 2006, ApJ, 639, 157
Wu, Y., Charmandaris, V., Hunt, L. K., et al. 2007, ApJ, 662, 952 (Wu07)

Online Material

Appendix A: Models for other GEHIIRs

Models of GEHIIRs include studies of individual objects and evolutionary sequences for large samples. Examples ordered by decreasing O/H are reviewed.

A.1. Individual GEHIIRs

A.1.1. O/H $\geq 1.5 \times 10^{-4}$

González Delgado & Pérez (2000) successfully model NGC 604 (O/H = 3×10^{-4}) in M 33 as a radiation-bounded sphere (radius 20−110 pc) of density 30 cm^{-3} and filling $\epsilon = 0.1$, both [O I]λ 6300 and [O III]λ 4363 being explained.

García-Vargas et al. (1997) successfully model circumnuclear GEHIIRs in NGC 7714 as thin, constant-density ($N_{\rm H} \sim 200$ cm^{-3}), radiation-bounded shells with O/H = $(2-3) \times 10^{-4}$: r([O III]) is accounted for within errors and [O I] is just moderately underestimated. The nuclear GEHIIR of NGC 7714 is modelled by González Delgado et al. (1999) as a full sphere with very small ϵ. The adopted O/H = 3×10^{-4} is too large since [O III]λ 4363 is underpredicted. Obviously, a better fit to the available optical line spectrum could be achieved for the nucleus. González Delgado et al. (1999) are probably not well founded to invoke extra heating by shocks.

Luridiana & Peimbert (2001, LP01) propose a photoionization model for NGC 5461 (O/H = 2.5×10^{-4}), a GEHIIR in M 101. As for NGC 2363 (Appendix A.1.2), LP01 apply an aperture correction to their spherical model. The Hβ and r([S II]) spatial profiles are reproduced with a Gaussian density distribution of very small ϵ and high inner density – 500 cm^{-3} compared to $N_{\rm e}$([S II]) $\sim$ 150 cm^{-3} – meant to increase the inner O^+ fraction. In this way, the λ 5007, λ 4363 and λ 3727 fluxes restricted to the theoretical slit can be accounted for[5], but not [O I], "a not unusual fact", nor [S II], which, against a statement of LP01, is not enhanced by increasing the primary flux below 1.0 ryd. As noted by LP01, the outputs of their model are strongly dependent on the density structure.

From their sophisticated study of NGC 588 (O/H = 2×10^{-4}), Jamet et al. (2005, JS05) conclude that "the energy balance remains unexplained". This negative conclusion is based on the fact that $T_{\rm e}$([O III]), from the ratio λ 4363 Å/λ 5007 Å, is observed to be larger than $T_{\rm e}$([O III], IR), from λ 5007 Å/λ 88 μm, by $\Delta T_{\rm obs} = 2700 \pm 700$ K, while the corresponding $\Delta T_{\rm mod}$ is only 1400 ± 200 K in models which are otherwise satisfactory, accounting reasonably well for $T_{\rm e}$([O III]) and the distribution of ionization (models DD1 and DDH exhibited by JS05, who carefully consider uncertainties related to the SED and the small-scale gas distribution). Considering the difficulty of calibrating the ISO-LWS fluxes relative to the optical and the sensitivity of the [O III]λ 88 μm emissivity to $N_{\rm e}$, the 400 K gap between $\Delta T_{\rm obs}$ and $\Delta T_{\rm mod}$ is not a sound basis to claim the existence of an energy problem. If diagnostics based on IR lines are desirable, the energy problem raised so far in GEHIIR studies is not related to these lines. Instead of a heating problem as in I Zw 18, the model presented by JS05 could be facing a cooling problem, since the computed $T_{\rm e}$([O III], IR) is too high.

An additional energy source is not needed in the cases of NGC 588, NGC 5461, NGC 7714 and NGC 604.

[5] LP01 state a priori that [O III]λ 4363 "almost surely has a contribution from processes other than photoionization" and conclude that their model "fails to reproduce the observed [O III]λ 4363 intensity", but both statements seem to be refuted by evidence they present.

A.1.2. O/H $< 1.5 \times 10^{-4}$

Relaño et al. (2002) provide an inventory of NGC 346, a GEHIIR of the SMC (O/H = 1.3×10^{-4}). Their spherical, constant-density, matter-bounded photoionization model, whose only free parameter is a filling factor ϵ (*alla* SS99), accounts for the escape of ionizing photons, but underpredicts collisional lines, especially [O III]λ 4363. After unsuccessful variations on geometry, the authors preconize, following SS99, an additional source of energy.

After an extensive exploration of photoionization models with filling factor for the bright GEHIIR NGC 2363 (O/H = 8×10^{-5}), Luridiana et al. (1999, LPL99) conclude that they cannot find a solution unless they introduce $T_{\rm e}$ fluctuations by hand, i.e., they assume a larger t^2 than the one intrinsic to their model. This t^2, intended to enhance the computed [O III]λ 4363, is justified by the fact that the observed Paschen jump temperature is less than $T_{\rm e}$([O III]) and supported by a self-consistency argument: a larger t^2 leads to a larger O/H, hence a larger number of WR stars, hence (1) a larger injection of mechanical energy, supposed to feed the temperature fluctuations themselves, and (2) a higher photon flux above the He^+ ionization limit, useful to increase He IIλ 4686. However, as acknowledged by Luridiana et al. (2001), the WR star winds generate an insufficiently large t^2 in NGC 2363. Also, present views suggest that arguments based on WR stars in low-Z galaxies were false (e.g., Leitherer 2006; Appendix C). Finally, r([O III]), underestimated by only ∼12% in the "standard" low-Z model by LPL99, is divided by 2 on using the larger O/H, so that a relatively minor difficulty is made much worse and then solved by means of an arbitrary t^2. The slit correction advocated by LPL99 is considered in Appendix B.2.

Luridiana et al. (2003, LPPC03) consider a spherical model for a GEHIIR of SBS 0335-052 (O/H = 2×10^{-5}). A Gaussian distribution with high maximum density and small ϵ proves unsatisfactory. LPPC03 then consider a 10-shell model (over 50 free parameters, most of which are pre-defined), in which each shell is radiation bounded and is characterized by a covering factor. Although each shell is still given an ϵ, the new model is equivalent to a collection of geometrically thin radiation-bounded sectors at different distances from the source (see also Giammanco et al. 2004) and "gracefully reproduces the constancy of the ionization degree along the diameter of the nebula". Hence, the authors are forced by observational evidence to implicitly abandon the classical filling-factor approach. Nonetheless, whatever the complexity of these models, all of them fail to account for the high $T_{\rm e}$([O III]).

LPPC03 consider a Gaussian model for I Zw 18 SE (O/H = 1.7×10^{-5}) with again a relatively large maximum density and, unlike for SBS 0335-052, a relatively large ϵ, resulting in a rather compact model nebula, in which the computed $T_{\rm e}$([O III]) compares quite well with the observed one. Unlike for the NW, the HST image (Cannon et al. 2002) of the younger SE H II region does not show a shell surrounding an MSC. Nonetheless, considering the strong output of mechanical energy from massive stars, it is likely that inner cavities already developed. The strong indirect evidence for too compact a gas distribution in the model by LPPC03 is the notable weakness of the computed intensity of [O II] and other low-ionization lines. Adopting a more expanded structure in order to increase [O II], yet keeping the general trend of the gas distribution, the computed $T_{\rm e}$([O III]) would be forseeably lower than in the model by LPPC03.

Previous photoionization models for low oxygen abundance GEHIIRs appear to systematically fail.

A.2. Individual GEHIIRs: discussion

LPPC03 describe the "T_e([O III]) problem" they face in their study of SBS 0335-052 (Appendix A.1.2) as "a systematic feature" of H II region models and, following SS99, they state that this problem "can be ascribed to an additional energy source acting in photoionization regions, other than photoionization itself". Nevertheless, T_e([O III]) seems to be accountable in existing photoionization models for GEHIIRs with, say, O/H $\geq 1.5 \times 10^{-4}$ (Appendix A.1.1). Similarly, the computed [O III]λ 4363 is correct, possibly even too large, for H II regions of the LMC (Oey et al. 2000). If, despite apparent complementarities, the T_e([O III]) and t^2 problems have different origins (Sect. 1), no "systematic feature" can be invoked.

In modelling near solar abundance GEHIIRs, [O III]λ 4363 is controlled by O/H, [O III]λ 5007 by the "color temperature" of the ionizing radiation, [O II]λ 3727 by the ionization parameter, while [O I] is maximized in radiation-bounded conditions. For these objects, assuming a "large" (constant) density, e.g., $\geq N_e$([S II]), associated with an ad hoc $\epsilon \ll 1$, is often successful, although this does not prejudge the relevance of the model found. Indeed, this assumption proves to be at the heart of the T_e([O III]) problem met in low-Z BCDs (Appendix B.1).

A.3. Extensive analyses of BCDs

The conclusion of an early extensive analysis based on radiation-bounded, low-density full sphere models for low-Z BCDs (Stasińska & Leitherer 1996) is optimistic concerning T_e([O III]), whereas [O I] is then qualitatively explained in terms of shock heating. Nevertheless, in an extension of this study to large-Z objects with no measured T_e([O III]), Stasińska et al. (2001) reinforce the energy problem raised by SS99 (Sect. 2.2) when they conclude that "a purely "stellar" solution seems now clearly excluded for the problem of [O III]/Hβ versus [O II]/Hβ as well as [S II]/Hβ", while, conversely, they still endorse the unproved statement of SS99 (Sect. 2.3) that "strong [O I] emission is easily produced by photoionization models in dense filaments".

The sequence of photoionization models proposed by Stasińska & Izotov (2003, SI03) for a large sample of low-Z BCDs (divided in three abundance bins) illustrates views expressed after the failure of models acknowledged by SS99 for I Zw 18 (Sect. 2). In the description by SI03, an evolving synthetic stellar cluster (10^5 $M_\odot$, instantaneous burst) photoionizes a spherical shell of constant density $N_H = 10^2$ cm^{-3} at the boundary of an adiabatically expanding hot bubble. With suitable bubble properties, underlying old stellar population, aperture correction and time evolution of the covering factor, the range of Hβ equivalent width (EW(Hβ)) and the trends of [O III] 5007, [O II] 3727, [O I] 6300 versus EW(Hβ) can be reproduced for the high-Z bin (O/H $\sim 1.5 \times 10^{-4}$) within the scatter of the data.

Applying similar prescriptions to the intermediate-Z bin, the oxygen lines and He IIλ 4686 (He II was just fair in the first bin) are underpredicted. SI03 diagnose an insufficient average energy per absorbed photon and assume that the stellar cluster is supplemented by a strong 10^6 K bremsstrahlung-like radiation source, which solves the He II problem (He^+ is further ionized by extra 4−5 ryd photons; see, however, Appendix C) and alleviates the [O I] problem (the soft X-rays further heat and widen the ionization front), but barely improves [O III] and [O II]. Agreement of the model sequence with observation is finally restored by supposing in addition that the shell includes a time-variable oxygen-rich gas component attributed to self-enrichment: in the example shown by SI03, this component is 4-fold enriched in CNO, etc. relative to the original abundance and encompasses half of the shell mass after a few Myrs, so that one generation of stars produced a 2.5-fold enhancement of the average abundance in the photoionized gas.

This description essentially applies to the low metallicity bin (O/H $\sim 2 \times 10^{-5}$) of particular concern for I Zw 18, but with even more extreme properties for the O-rich component, since it should be overabundant by 1 dex, resulting in a 5-fold enhancement of the final average abundance.

A.4. Extensive analyses of BCDs: discussion

The time scale of 0.5 Myrs for the growth of the O-rich component in the description by SI03 cannot directly fit in the self-pollution scenario since it is shorter than the stellar evolution time scale. Also, a sudden oxygen self-pollution of the gas is not observed in supernova remnants.

The assumed X-ray power is ∼10% of the cluster luminosity or ∼2 dex times the estimated X-ray ROSAT power (0.07−2.4 keV) of the hot bubble fed by stellar winds and supernovae around a usual MSC (Strickland & Stevens 1999; Cerviño et al. 2002). Moreover, the hot gas is generally raised at several 10^6 K (Stevens & Strickland 1998). Adopting a larger temperature, the X-ray power should be even larger, as only the softer radiation interacts usefully with the ionized gas. I Zw 18 itself is a rather strong X-ray emitter in the 0.5−10 keV range, yet 20 times weaker than the source assumed by SI03 (Thuan et al. 2004; Sect. 6.5).

Apart from these problems, SI03 do not address the question of the intensity of [O III]λ 4363. The narrow radiation-bounded shell adopted by SI03 usefully favours [O I]λ 6300, but makes the computed intensity of [O III]λ 4363 even worse than the one obtained by, e.g., SS99 (Sect. 2). Moreover, adding the prominent O-rich component advocated by SI03 will (1) decrease [O III]λ 4363 by a further 30−40% on average and (2) conflict with the existence of very low-Z BCDs, since any of them will shift to the intermediate class defined by SI03 after 1−2 Myrs.

If what SI03 qualify as "appealing explanations" are necessary for BCD models, then the hypothesis of photoionization by stars, which was already given a rough handling by SS99 in their analysis of I Zw 18, should be considered as definitively excluded for the whole class of low-Z BCDs. The fact that SI03 discard [O III]λ 4363 in their analysis confirms that they endorse and reinforce views expressed by SS99 or Stasińska et al. (2001) and give up explaining T_e([O III]) in low-metallicity GEHIIRs by means of stellar radiation. However, the same restrictive assumption as for individual GEHIIR studies (Appendices A.1−A.2) bears on the gas distribution adopted by SI03, since their (geometrically thin) "high" constant-N_H model sphere is a zero-order approximation of a model shell with a classical filling factor (Appendix B.1).

Appendix B: The gas distribution in GEHIIRs

B.1. The filling factor concept

To reproduce the Hα surface brightness of H II regions, asssuming a gas density much larger than $\langle N_e{}^2 \rangle^{1/2}$, the "filling factor paradigm" posits that the emitting gas belongs to *optically thin*, "infinitesimal" clumps, filling a fraction $\epsilon \ll 1$ of the volume.

Given that the stellar evolution timescale exceeds the sound crossing time of H II regions, small optically thin ionized clumps will have time to expand and merge into finite-size structures. If

these structures are assumed to have the original density, they are likely to have finite or large optical depths, in contradiction with the filling factor concept.

Filamentary structures, ubiquitous in Hα images of nearby GEHIIRs, are often taken as justification for introducing ϵ in photoionization models. However, (1) the geometrical thickness of observed filaments is consistent with radiation-bounded structures and (2) an individual filament most often emits both high and low ionization lines (e.g., Tsamis & Péquignot 2005). The filling-factor description is flawed.

A GEHIIR may well be a collection of radiation-bounded filaments embedded in coronal and photoionized diffuse media. The idea behind assuming this configuration is that only the ionized "atmospheres" of long-lived, radiation-bounded, evaporating structures will maintain a substantial thermal overpressure relative to their surroundings (a similar idea applies to the "proplyds" found in Orion; e.g., Henney & O'Dell 1999).

The filling factor concept fails on both theoretical and observational grounds. Nevertheless, introduced as a technical tool to manage $N_{\rm e}$ diagnostics like r([S II]), ϵ came to be improperly used to adjust the local ionization equilibrium of the gas through $N_{\rm H}$, in an effort to overcome problems of ion stratification generated by the filling factor description itself (Appendix B.2).

The $T_{\rm e}$([O III]) problem met in oxygen-poor GEHIIRs may relate to the loss of plasticity affecting photoionization models, as the dependence of gas cooling on abundances vanishes. Then, cooling depends on the relative concentration of H^0 (collisional excitation of Lyα), *controlled by the local* $N_{\rm H}$. Hence, the (improper) freedom on ϵ is eroded. Moreover, if the density is not uniform, $N_{\rm e}$([S II]) is a biased estimate for $N_{\rm e}$ in the bulk of the emitting gas, since S^+ ions will belong to dense, optically thicker clumps. Emission from an interclump medium with $N_{\rm e} < N_{\rm e}$([S II]) will selectively enhance the computed [O III]λ 4363 intensity. LPL99 state that their model includes "denser condensations uniformly distributed in a more tenuous gas", but in practice only the condensations emit. This restriction is shared by virtually all published models for low-Z GEHIIRs. While the assumed density of the emitting gas can be orders of magnitude larger than $\langle N_{\rm e}^2\rangle^{1/2}$, emission from a lower density gas is neglected by construction (The study by JS05 is an exception, but NGC 588 is not low-Z; Appendix A.1.1). The $T_{\rm e}$([O III]) problem suggests lifting this restriction.

B.2. Spheres, slits, filling factor and stratification

Spherical models raise the question of how to compare computed spectra with nebular spectra observed through, e.g., a narrow slit. LPL 99 (Appendix A.1.2) advocate extracting emission from that part of the sphere which would project on the slit. Despite obvious problems with non-sphericity, LPL 99 and others argue that this procedure would at least allow weighting the contributions from low- and high-ionization zones in a more realistic manner. Using the classical filling factor concept (Appendix B.1) in GEHIIR models, ion stratification spreads over the whole nebula and the [O I] emission is effectively confined to outer layers, in which the primary radiation eventually vanishes. If, on the contrary, the emitting gas belongs to radiation-bounded filaments distributed within the nebula, then ion stratification disappears to first order. Radial ionization gradients, if any, are no longer related to a progressive destruction of primary photons along the full radial extension of the nebula, but to changes in (local) average ionization parameter.

LPL 99 conclude that [O I] is due to shock excitation in NGC 2363 because the computed intensity is weak in their theoretical slit extraction. Nonetheless, the [O I] intensity is fairly correct in their global spectrum. This apparent failure of their photoionization model may be due to the unfortunate combination of (1) a very small ϵ and (2) the extraction of a slit shorter than the diameter of the model sphere. Along the same lines, LPPC03 are confronted with undesirable consequences of the filling factor assumption on the variation of ionization along a slit crossing SBS 0335-052 (Appendix A.1.2).

If a geometrically defined model can hardly provide an approximation to a complex H II region, thus casting doubt on theoretical slit extractions, global spectra are less sensitive to geometry, because of conservation laws.

Moreover, in computing 1D photoionization models, the (spherical) symmetry enters only in the treatment of the diffuse ionizing radiation field, which is generally not dominant in the total field. The diffuse field, most effective just above the ionization limits of H, He and He^+, is relatively local at these photon energies (in accordance with the "Case B" approximation) and little dependent on global geometry. Let us define an "elementary spherical model" (for given SED) as a radial density distribution of whatever complexity. Since the local state of the gas is chiefly related to the primary (radial) radiation, a composite model made of a judicious combination of elementary spherical models, each of them restricted to a sector characterized by a covering factor, can provide topologically significant and numerically accurate descriptions of global spectra for nebulae with complex structures. Defining a "topology" as a particular set of spherical models with their attached covering factors, any given topology is in one-to-one correspondence with a global spectrum and a full class of geometries, since any sector can be replaced by an arbitrary set of subsectors, provided that the sum of the covering factors of these subsectors is conserved.

Thus, a good modelling strategy for a GEHIIR is one in which a global (probably composite) model spectrum is compared to the observed global spectrum. If only one slit observation is available, given that the ion stratification tends to be relatively loose and erratic in GEHIIRs, it is wise to directly use this spectrum as the average spectrum (together with scaling by the absolute Hβ flux), with the understanding that the resulting photoionization model will represent a "weighted average" of the real object. For many practical purposes, this weighting may not significantly impact on the inferences made from the model, unless the slit position is largely unrepresentative.

Appendix C: He IIλ 4686, WR stars and SEDs

I Zw 18 harbours Wolf-Rayet (WR) stars (Legrand et al. 1997; Izotov et al. 1997a; de Mello et al. 1998; Brown et al. 2002). WR stars have been challenged as the sole/main cause of nebular He IIλ 4686 in BCDs on the basis of a lack of correlation between the occurence of this line and the broad "WR bumps" (e.g., Guseva et al. 2000). The study of WR stars is experiencing a revolution (Maeder et al. 2005; Meynet & Maeder 2005; Gräfener & Hamann 2005; Vink & de Koter 2005; Crowther 2007) after the realization that (1) rotation of massive stars favours enhanced equatorial mass loss, element mixing by shears, and angular momentum transport by meridian circulation, (2) low-Z massive stars tend to be fast rotators and accelerate as they evolve off the main sequence, so that the lower mass limit for a star to become a WNE star is much reduced, and (3) for a given type of WR star, the mass loss is lower for lower metallicity (Fe/H, not O/H), with three consequences: the broad WR features are less evident for low metallicity (weaker optical continuum and smaller EW of WR bumps), the duration of the

WR stage can be longer, and the EUV luminosity is larger due to a reduced blanketing effect. Thus, the above lack of correlation can now be partly ascribed to a bias, related to the tendency of WR star atmospheres to display less prominent optical signatures when they emit more EUV radiation. The WR star population of I Zw 18 and the ability of these stars to emit radiation beyond 4 ryd have almost certainly been grossly underestimated (Crowther & Hadfield 2006).

Other observations, e.g., for SBS 0335 052E (Izotov et al. 2001b, 2006b) are still taken as evidence for He II excitation by radiation from very fast shocks: (1) the He II line is broader than other nebular lines; (2) the He II emission is spread out far away from the main MSCs; and (3) T_e is larger in the He II emitting area, hence at large distances from the main ionizing sources. These findings are not compelling arguments against photoionization by WR stars. The larger He II line width indicates greater turbulence and/or velocity gradients, not necessarily shocks. That T_e is observed to be larger in He II emitting gas is in agreement with photoionization models. The spatial extent of He II may reflect the distribution of a few WR stars, which may not belong to the main cluster and may not be easily detected (Crowther & Hadfield 2006). Alternatively, He II can be produced far from the ionizing stars if the medium is porous and permeated by low density, optically thin gas, e.g., along a galactic wind outflow (Izotov et al. 2006b). The picture of a galactic wind also suggests an explanation for the He II width.

Photoionization models are test beds for ionizing radiation sources, but inferences about the physics of GEHIIRs should not depend on uncertain SEDs. Existing synthetic star clusters are inadequate to model I Zw 18. Apart from known problems with star sampling (Cerviño et al. 2003; Cerviño & Luridiana 2006), limited knowledge of the history of actual MSCs and current uncertainties about WR stars, new free parameters (initial angular momentum and magnetic field of individual stars; rate of binarity) will broaden the range of possible SED evolutions, while collective effects in a compact cluster of massive stars may influence the output of ionizing radiation far from it, due to high-density stellar winds (Thompson et al. 2004).

These comments justify (1) the assumption of an excitation of He II solely by WR stars and (2) the use of a flexible analytical SED for I Zw 18 NW (Sect. 4.1).

Table D.1. Effective collision strengths for [O III].

$T_e/10^4$ K:	0.5	1.0	2.0	3.0
Reference:[a]		$\Omega(^3P-{}^1D)$		
Sea58	–	1.59	–	–
SSS69	–	2.39	–	–
ENS69	1.85	2.50	2.91	2.96
ES74	2.17	2.36	2.55	–
Men83	2.02	2.17	2.39	–
Ag83	2.035	2.184	2.404	2.511
BLS89	2.10	2.29	2.51	2.60
Ag93	2.039	2.191	2.414	2.519
LB94	2.1268	2.2892	2.5174	2.6190
AgK99[b]	2.0385	2.1906	2.4147	2.5191
LB94/AgK99[c]	1.0435	1.0450	1.0425	1.0397
		$\Omega(^3P-{}^1S)$		
Sea58	–	0.220	–	–
SSS69	–	0.335	–	–
ENS69	0.255	0.298	0.331	0.339
ES74	0.276	0.325	0.356	–
Men83	0.248	0.276	0.314	–
Ag83	0.2521	0.2793	0.3162	0.3315
BLS89	0.260	0.287	0.318	0.331
Ag93	0.2732	0.2885	0.3221	0.3404
LB94	0.2720	0.2925	0.3290	0.3466
AgK99[b]	0.2732	0.2885	0.3221	0.3404
LB94/AgK99[c]	0.9956	1.0139	1.0214	1.0182
		$\Omega(^1D-{}^1S)$		
Sea58	–	0.640	–	–
SSS69	–	0.310	–	–
ENS69	0.483	0.578	0.555	0.510
ES74	0.807	0.856	0.752	–
Men83	0.516	0.617	0.634	–
Ag83	0.5463	0.6468	0.6670	0.6524
BLS89	0.59	0.677	0.664	0.634
Ag93	0.4312	0.5227	0.5769	0.5812
LB94	0.4942	0.5815	0.6105	0.6044
AgK99[b]	0.4312	0.5227	0.5769	0.5812
LB94/AgK99[c]	1.1461	1.1125	1.0582	1.0399

[a] Refs: Sea58: Seaton (1958); SSS69: Saraph et al. (1969); ENS69: Eissner et al. (1969); ES74: Eissner & Seaton (1974); Men83: Mendoza (1983); Ag83: Aggarwal (1983); BLS89: Burke et al. (1989); Ag93: Aggarwal (1993); LB94: Lennon & Burke (1994); AgK99: Aggarwal & Keenan (1999).
[b] Results from Aggarwal (1993).
[c] Collision strength ratio.

Appendix D: Atomic data

D.1. Collisional excitation of HI

Collision strengths $\Omega(1s–nl)$ ($n < 6; l < n$) for H I are taken from Anderson et al. (2000, ABBS00). The Ωs for $1s–2s$ and $1s–2p$ are much larger than for the next transitions $1s–nl$ and are not controversial. The main cooling agent in low-Z BCDs should be correctly implemented in all codes. Nonetheless, in the conditions of I Zw 18, the results for transitions 1–2 by ABBS00 are about 10% larger than those carefully fitted by Callaway (1994), giving an estimate of possible uncertainties. The adopted data tend to enhance the cooling with respect to earlier data and to (conservatively) worsen the "T_e([O III]) problem". Total $\Omega(1–n)$ listed by Przybilla & Butler (2004) virtually coincide with ABBS00 values for 1–2, confirming the H I cooling rate, but diverge from ABBS00 for $n > 2$ and increasing T_e similarly to early, probably wrong, data (see Péquignot & Tsamis 2005).

D.2. Collisional excitation of [OIII]

Effective collision strengths Ω obtained over the past 50 years are listed in Table D.1 at four T_e for transitions $^3P-{}^1D$, $^3P-{}^1S$ and $^1D-{}^1S$. Aggarwal & Keenan (1999) did not feel it necessary to update earlier values by Aggarwal (1993; Ag93), almost contemporary with Lennon & Burke (1994). The ratios of the recent values are given in Table D.1. The differences are over 4% for $^3P-{}^1D$ and 10% for $^1D-{}^1S$ (6% in I Zw 18 conditions), but the latter has no influence at low N_e. NEBU includes a fit better than 0.5% to Ag93 data.

The [O III] transition probabilities used in NEBU are from Galavis et al. (1997, GMZ97). The accuracy of the Opacity Project (OP) data for these transitions is 8–10% (Wiese et al. 1996). Coherently, the much more elaborate results by GMZ97 differ from the OP results by 9.6% and 5.5% for $A(^1D-{}^1S)$ and $A(^1P-{}^1S)$ respectively. Would $A(^1D-{}^1S)$ change by as much as 5%, the branching ratio of [O III]λ 4363 would change by 0.6%.

Thus, discrepancies not exceeding 5% exist among different calculations (3% for Ω ratios), suggesting that uncertainties on the computed r([O III]) are probably <5%. The 25−30% underestimation found by SS99 is not due to erroneous atomic data.

D.3. Miscellaneous data

The adopted table for radiative and dielectronic recombinations is limited to the 11 sequences that are H-like−Na-like (Badnell 2006). Dielectronic rates for [S II]−[S IV] are given by Badnell (1991), but total recombination coefficients for (recombined ions) [Si II], [S II], [S III], [Ar V], [Fe II]−[Fe V], are taken from Nahar and co-workers (Nahar 2000, and references cited). The recombination rate for [S II] used in this and previous NEBU computations is 1.15 times the Nahar value. Empirical total rate coefficients based on planetary nebula models (Péquignot, unpublished), implemented in NEBU for a decade, are 5 and 8 times the radiative ones for [Ar II] and [Ar III] respectively. A larger factor is suspected for [Ar III] at high T_e.

Collision strengths of special mention include those for [O II] (Pradhan et al. 2006; also Tayal 2006b), [O IV] (Tayal 2006), [S III] (Tayal & Gupta 1999), [S IV] (Tayal 2000) and [Fe V] (Wöste et al. 2002). Collisions with H^0 are considered in Sect. 6.5. Charge exchange rates with H^0 for O^{2+} and N^{2+} are now from Barragán et al. (2006).